Supporting Information for

Design Principles for Photonic Crystals Based upon Plamonic Nanoparticle Superlattices

Lin Sun[a,b] Haixin Lin[b,c], Kevin L. Kohlstedt[c], George C. Schatz[1,b,c] & Chad A. Mirkin[1,a,b,c]

[a]Department of Materials Science and Engineering, [b]International Institute for Nanotechnology, [c]Department of Chemistry, Northwestern University, Evanston, IL 60208 USA

[1]Email: chadnano@northwestern.edu; g-schatz@northwestern.edu.

This Supporting Information contains:

www.pnas.org/cgi/doi/10.1073/pnas.1800106115

1. Materials and Methods

1.1 Finite-Difference Time-Domain (FDTD) Simulation

FDTD simulations were run with a commercial package Lumerical FDTD Solutions v.8.12.631. The dielectric functions of gold, silver, aluminum and copper were adopted from the experimental data obtained by Johnson and Christy (1), Shiles *et al.* (2) and Hagemann *et al.* (3), respectively. The refractive index of silica was assumed to be 1.46. In order to obtain the reflectance spectra, an infinite thin slab model was used, unless otherwise specified, where periodic boundary conditions were adopted in the x and y directions such that a simple cubic unit cell was repeated infinitely in the x-y plane. A perfectly matched layer boundary condition was used in the z direction, which was also the light propagation direction. The length of the superlattice in the z direction was determined by the number of layers and the lattice constant in the z direction. The infinite thin slab model assumes that only the center of the reflected light is collected, namely not counting light reflected at the edge and side of the photonic crystals. The validity of this model for our experimental setup and DNA-nanoparticle (NP) superlattice was previously demonstrated in the literature (4). Illumination with light occurs in air ($n_0 = 1$), and the crystal is assumed to lie on top of a glass substrate ($n_s = 1.44$). For band-structure calculations, a single unit cell for the simple cubic lattices and four unit cells for the diamond lattice were simulated with Bloch boundary conditions. More than ten dipole sources with random orientation and location within the simulation region were used to excite all optical modes in the lattices. More than ten randomly located time monitors were used to collect the signal in the time domain, and Fourier transform was performed to convert data into the frequency domain.

1.2 Nanoparticle Synthesis and Characterization

Gold nanocubes (88 nm edge length, >95% were cube shaped with a <5% variation in size) were synthesized according to a seed-mediated method (5). The uniform seeds prepared *via* iterative reductive growth and oxidative dissolution reactions are critical to the uniformity of the final products. Particle uniformity was characterized based on statistical analysis of Hitachi H8100 transmission electron microscope (TEM) images (Fig. S1).

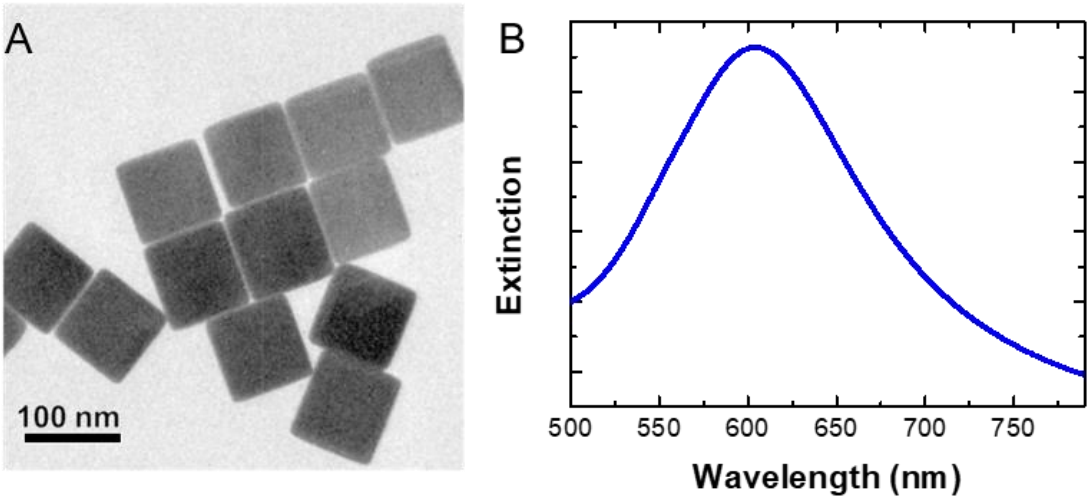

Fig. S1. Characterization of 88 nm nanocubes. A representative TEM image (*A*) and UV-Vis spectrum (*B*) of the monodisperse nanocubes.

1.3 DNA Design, Synthesis and Purification

DNA strands used in this work were designed according to the literature recommendations (6, 7). Detailed DNA sequences can be found in Table S1. They have three key components: an anchor strand, a linker strand, and duplexer strands. The anchor strand with a thiol group allows them to be adsorbed onto gold nanoparticles, a dA_{10} region that increase the flexibility (light gray) (8), and a region that can hybridize to the linker strand (dark gray). The linker strand contains three regions: an 18-base sequence (dark blue) complementary to the dark gray region of the anchor strand; some repeated 40-base spacer sequences (dark green) which are designed for conveniently controlling the length of the "DNA bonds"; and a 4-base self-complementary sticky end (light blue) which determines the interaction between the assembling nanoparticles. Each region is separated by a single base A to provide some flexibility. The duplexer strands (light green) can hybridize to the 40-base spacer sequences in the linker strand (dark green).

Table S1. DNA sequences used in this work. The three regions of linker strand are highlighted with different color.

	DNA sequence (5'–3')	Number of base
Anchor strand	TCA ACT ATT CCT ACC TAC AAA AAA AAA A SH	28
Linker strand	GTA GGT AGG AAT AGT TGA A TTTTTTTTTTTT ACT GAG CAG CAC TGA TTTTTTTTTTTT A GCGC	64
Duplexer strand	AAAAAAAAAAAAA TCA GTG CTG CTC AGT AAAAAAAAAAAA	40

DNA strands in this work were synthesized with a MM48 synthesizer (BioAutomation) on a solid-support with reagents purchased from Glen Research and purified via reverse-phase high-performance liquid chromatography (HPLC; Agilent). Matrix-assisted laser desorption ionization time-of-flight mass spectrometry (MALDI-

TOF-MS) was used to confirm the molecular weight and purity of HPLC-purified DNA. Concentration was determined by UV-vis spectrometry. The extinction coefficient of each DNA strand was calculated with OligoAnalyzer tool from Integrated DNA Technologies.

1.4 Nanoparticle Functionalization and Assembly

Nanocubes were chemically functionalized with anchor strand through literature procedures (6, 7, 9). The as-synthesized nanocubes were collected by centrifugation and washed with H_2O. This process was repeated. After removing the supernatant, the colloid was re-dispersed in an aqueous solution of the desalted anchor strand (2 OD_{260} of DNA for 1 OD_{SPR} of nanocube). Note that this strand prior to use was maintained in the reduced state with dithiolthreitol (DTT, Sigma Aldirich). Both the DTT and salt must be removed prior to particle modification (10). Then, the mixture was brought into 0.01 M phosphate buffer solution (PBS) and 0.01% sodium dodecyl sulfate (SDS) solution and was agitated on a shaker (~1000 rpm) for 0.5 hour. Then, the nanocubes were treated by slow addition of NaCl, which is leads to increased DNA loading (10). The salt concentration of the nanocube solution was successively increased from 0.05 M to 0.1 M to 0.2 M to 0.3 M to 0.4 M to 0.5 M NaCl using a 2 M NaCl stock solution. These additions were done sequentially with 10 s sonication and 0.5 hour shaking between each salt addition. The colloid was treated with overnight shaking after the final salt addition to insure maximum DNA loading. Free DNA strands were removed by three rounds of centrifugation with 0.01% SDS solution. The final pellet was re-suspensed in a solution contained 0.01% SDS, 0.01 M PBS and 0.5 M NaCl.

The DNA linker strand was mixed with duplexer strand in a solution containing 0.5 M NaCl and 0.01 M PBS, and then incubated at 40 ^{o}C for 0.5 hour for pre-hybridization. The duplexed DNA linker solution was then added into the functionalized nanocube colloid in excess to the amount of the anchor strands on particle surface. The mixture was allowed to incubate overnight at room temperature to form aggregates. 150 μL solutions with aggregates were pipetted into 150 μL PCR 8-tube strips (Life Technologies) and placed into a thermal cycler (Life Technologies). The temperature of the thermal cycler was first increased to 60 ^{o}C, and then slowly cooled to room temperature in a rate of 0.1 °C per 10 minutes. The slow cooling rate provides sufficient time for the superlattice to reach equilibrium during the assembly process (11).

1.5 Superlattice Characterization

Nanocube superlattices were embedded in silica before electron microscope, optical microscope and small angle X-ray scattering (SAXS) characterization. This method can preserve crystal symmetry and lattice parameter when superlattices are transferred from solvent (12). Scanning electron microscope (SEM; Hitachi SU8030) and scanning transmission electron microscope (Hitach HD2300) were used to observe the morphologies of nanocube superlattice. SAXS experiments, which reveal lattice parameters (Fig. S2), were performed at the DuPont-Northwestern-Dow Collaborative Access Team (DND-CAT) beamline of the Advanced Photon Source at Argonne National Laboratory. X-rays with λ= 1.24 Å (E = 10 keV) were used.

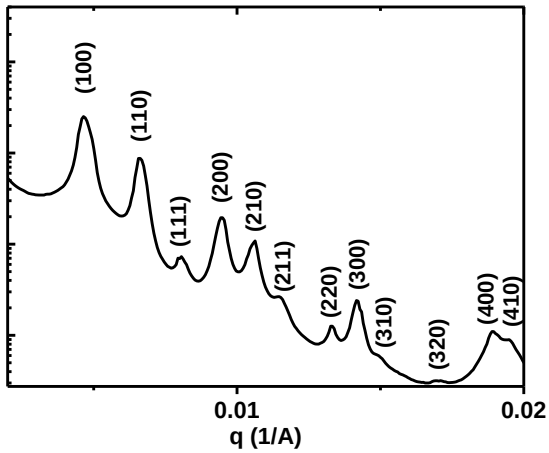

Fig. S2. SAXS data of nanocube superlattice. The lattice parameter of the nanocube superlattice is 134 nm based on the SAXS data.

1.6 Optical Measurements

Silica embedded superlattices (12) were first drop cast onto plasma cleaned Indium Tin Oxide (ITO) coated glass slides, and the solvent was fully evaporated, resulting in a population of superlattices with their flat surfaces lying parallel to the substrate. Superlattices were then observed and located with both a Zeiss Axio Observer.Z1 microscope and a Hitachi SU8030 SEM to ensure proper orientation and a flat top surface. A coverslip deposited with anti-reflection coating purchased from Evaporated Coatings Inc. is then fixed close to the sample by carbon tape at the corners. Subsequently, immersion oil with a refractive index matching that of silica was slowly injected in-between the coverslip and the glass slide, such that the samples were fully immersed in the oil. This effectively provides an optically homogeneous background for the silica-embedded superlattices. A Xenon lamp (XBO 75) with a broad-band spectrum (300 – 1100 nm) was used as the light source. In bright field (BF) reflection mode, the sizes of field-stop and aperture were minimized to minimize the angle of incident light. A 50× objective (N.A. 0.8) was used to collect light from only the center of the superlattices. A spectrometer with 50 g/mm grating (Princeton Instrument) and a charge coupled device (PyLoN) were connected to the microscope and were used to collect the backscattering spectra. A slit (50 μm) was used to extract the backscattering spectrum from a thin line at the center of the superlattice, which enables the use of the thin slab model in FDTD to simulate this system (4). Finally, a background spectrum was chosen from a clean region near the superlattice and was used to remove the signal from the background in the backscattering spectrum.

2. Considerations in Designing Photonic Crystals

In the one-dimensional case, the PC can be viewed as periodically alternating layers of high- and low-index materials or a distributed Bragg reflector (13), and the PBG can be identified as the spectral region with high reflectance (low transmittance) in the far-field spectra, in other words a stopband in the reflectance spectra. For incident angles perpendicular to the layers, the Bragg condition is best met when the optical length of each layer of the PC is a quarter of the relevant wavelength, equation (1).

$$\frac{\lambda_0}{4} = d_h n_h = d_l n_l \tag{1}$$

Here, λ_0 is the center wavelength of the photonic band, and d_h, n_h and d_l, n_l are the thicknesses and refractive indices of the high- and low-index materials, respectively (14). The higher the contrast between the high and low refractive indices, the broader the photonic band width, as governed by equation (2):

$$\frac{\Delta\lambda_0}{\lambda_0} = \frac{4}{\pi} \arcsin\left(\frac{n_h - n_l}{n_h + n_l}\right) \tag{2}$$

where $\Delta\lambda_0$ and λ_0 are the width and center frequency of the band (15). The maximum reflectance (R_{max}) is not only dependent on the index contrast but also on the number of layers through the equation:

$$R_{max} = \left[\frac{n_0 (n_h)^{2N} - n_s (n_l)^{2N}}{n_0 (n_h)^{2N} + n_s (n_l)^{2N}}\right]^2 \tag{3}$$

n_0 and n_s are the indices of the top and bottom layers outside of the crystal, and N is the number of layers of the high-index material (14).

For all of the fabrication methods for photonic crystals, a critical parameter for achieving large PBG and high reflectance is the refractive index contrast between the high- and low-index materials, the importance of which can be seen in equations (1)-(3) above (16-18). Moreover, as can be seen in equation (1), in order to satisfy the Bragg condition at certain wavelengths, the thickness of each layer can be reduced by using materials with a higher index, which is important for the miniaturization of devices.

3. Spectra of a Single Nanoparticle

For a systematic investigation of the effect of lattice parameters on the stopband features, FDTD simulations are performed where spherical Au NPs with 54 nm radius are arranged in a lattice structure, unless otherwise specified. Fig. S3 shows the absorption, scattering, and extinction spectra of a single spherical NP in silica host.

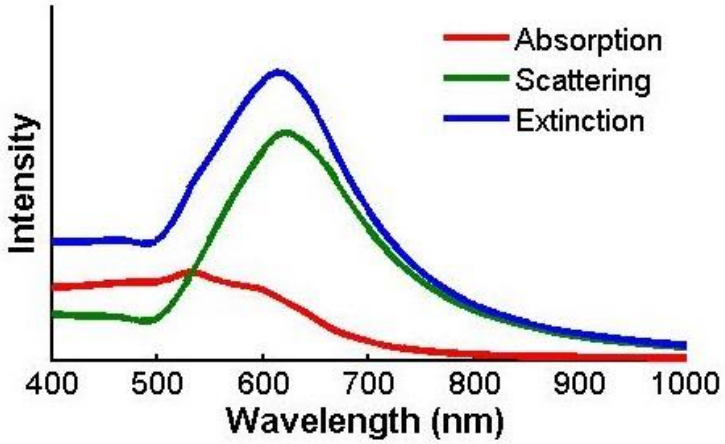

Fig. S3. Absorption, scattering, and extinction spectra of a single NP. The radius of the spherical NP is 54 nm. The NP is modeled to be in silica with a refractive index of 1.46.

4. Results for Cubic Superlattices

4.1 Effect of the number of NP layers

The dependence on N can be seen in Fig. S4, where the reflection spectra of superlattices with simple cubic (cP) lattice symmetry, 200 nm lattice constant but different number of layers (1 – 20) are shown. The stop band between 600 – 770 nm saturates at only 7 layers. However, as the lattice constants increases, more layers are needed for the reflection band to saturate (Fig. S5). To keep the computational time reasonable, the exact dependence on the number of layers is not examined, and 7 layers of superlattices are used (i.e. N = 7) in all simulations throughout the main text, unless otherwise specified.

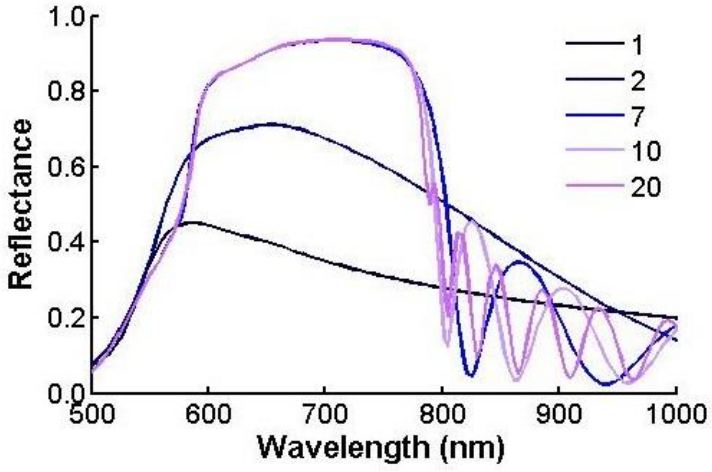

Fig. S4. Thickness dependence of the reflectance spectra. The spherical NP radius is 54 nm, and the crystal has simple cubic symmetry and a 200 nm lattice constant. The number of layers is shown in the legend. The reflectance spectra resemble that of dielectric photonic crystals. When there is only one layer, the structure is not periodic in the light propagation direction, thus no Bragg reflection occurs. As the number of layers increases, the reflection band appears and saturates quickly. The number of layers at which the stop-band saturates is 7 in this case.

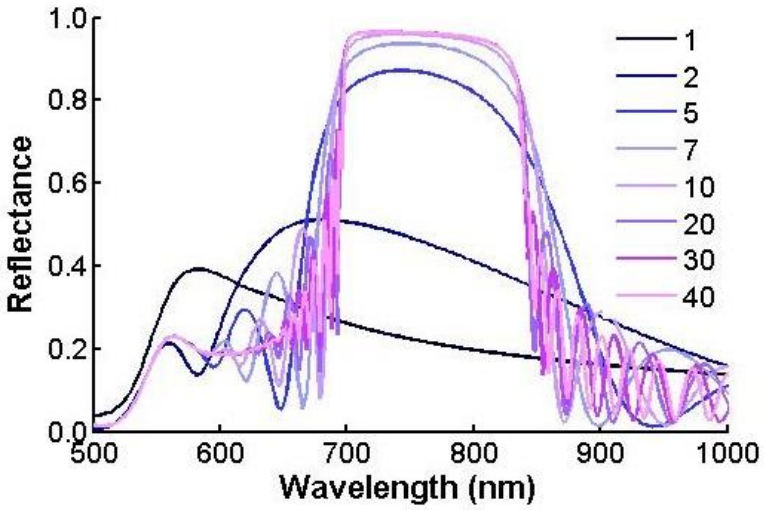

Fig. S5. Thickness dependence of the reflectance spectra of a crystal with larger lattice constant. The NP radius is 54 nm, and the crystal has simple cubic symmetry and a 240 nm lattice constant. Again, the number of layer is shown in the legend. In contrast with the superlattice with a smaller lattice constant (Fig. S4), the stop-band is not saturated until the number of layers exceeds at least 10.

4.2 Relationship between Stopband Features and Lattice Constant in a Cubic System

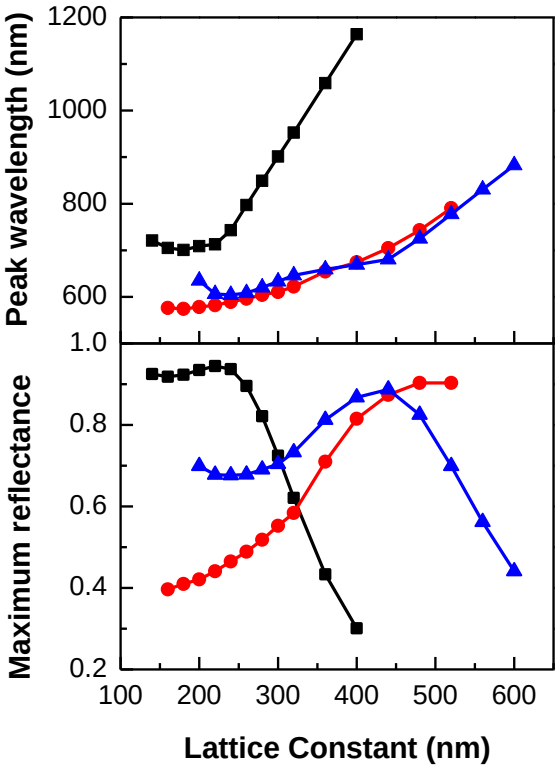

Fig. S6. Dependence of maximum reflectance and its corresponding wavelength on the lattice constant of cP, cI and cF lattices. The NP radius is 54 nm, and 7 layers are used. The spectra of these data points are shown below.

4.3 Reflectance Spectra of Cubic Superlattices

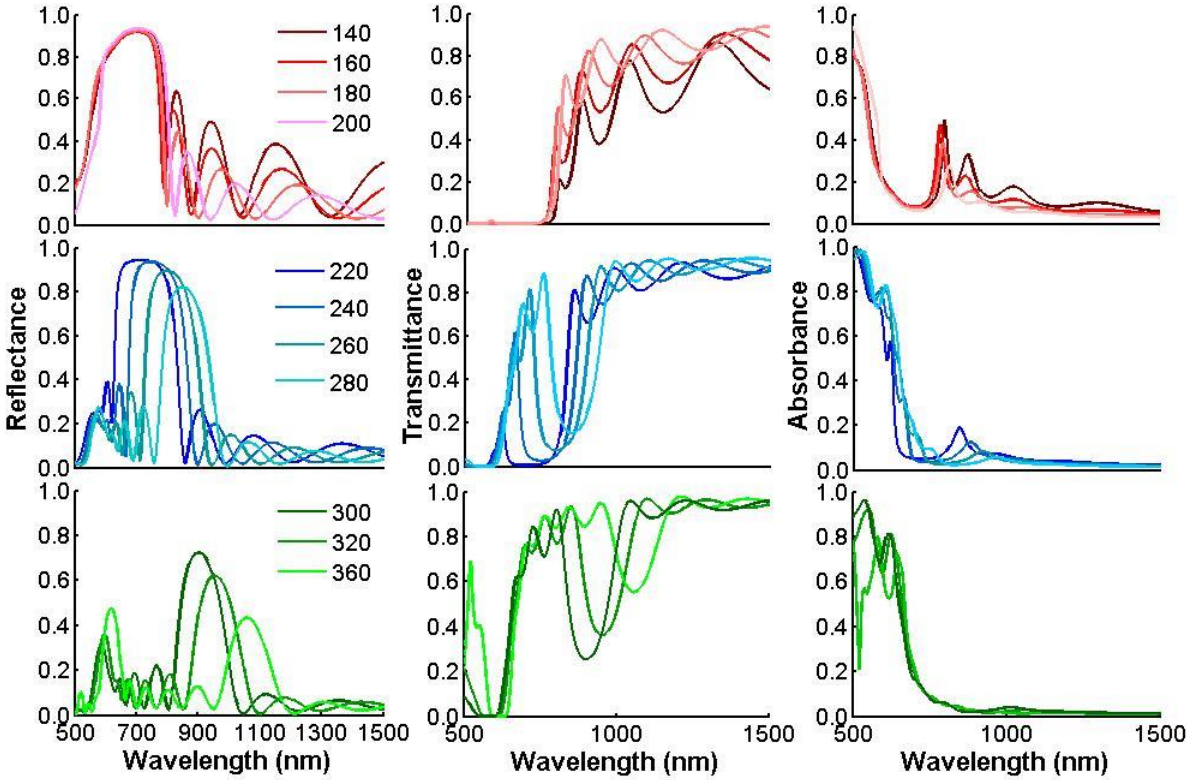

Fig. S7. Dependence on lattice constant of the reflectance, transmittance and absorbance spectra of cP lattices. The NP radius is 54 nm, and the layer number is fixed at 7. Lattice constants are shown in the legends. The range of lattice constants was chosen so that strong near-field coupling between NPs is avoided. As can be seen, the LSPR peak overlaps with the photonic band when the lattice constant is at or below 200 nm (top), while it is separated at a lattice constant equal to or larger than 220 nm (middle). When the lattice constant further increases beyond 300 nm, the first order peak further red shifts and a second order peak arises close to the LSPR (bottom).

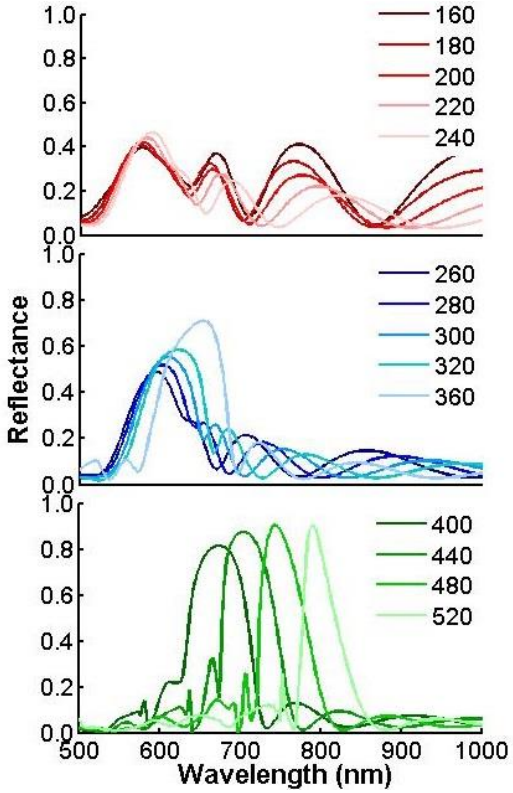

Fig. S8. The reflectance spectra dependence on lattice constant for cI lattices. The NP radius is 54 nm, and the lattices have 7 layers, namely 3 unit cells. Lattice constants are shown in the legends.

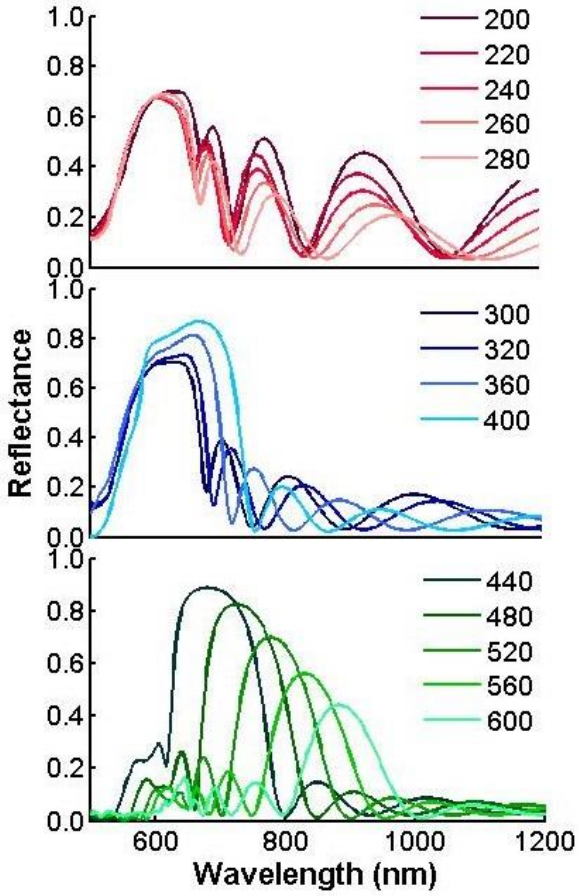

Fig. S9. Dependence on lattice constant of the reflectance spectra of cF lattices. The NP radius is 54 nm, and the lattices have 7 layers. Lattice constants are shown in the legends.

5. Results for Superlattices of Other Crystal Systems

5.1 Results of Tetragonal Superlattices

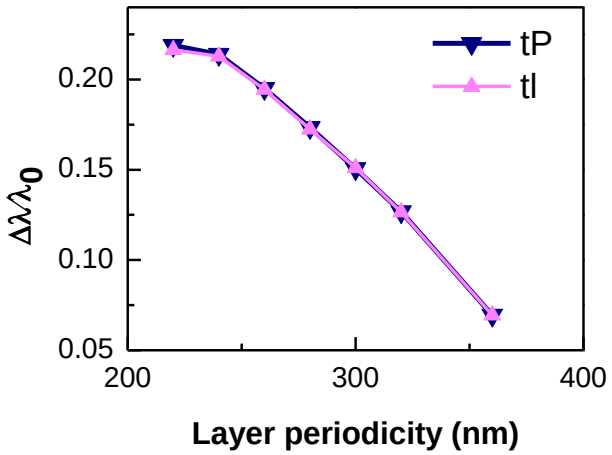

Fig. S10. Dependence of the bandwidth on the layer periodicity of tP and tI lattices. The NP radius is 54 nm, and the lattices have 7 layers. The lattice constant within each layer is kept at 200 nm. The reflectance spectra of the data points are shown below.

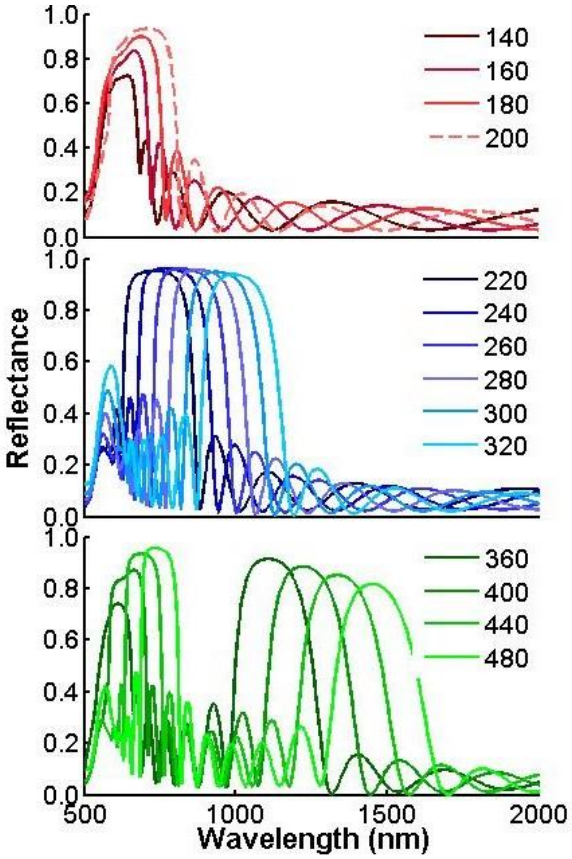

Fig. S11. Dependence on the layer periodicity of the reflectance spectra of tP lattices. The NP radius is 54 nm, and the lattices have 7 layers. Lattice constants in each metallic layer (*a*) is kept at 200 nm. Layer periodicities are shown in the legends. Interestingly, as the layer periodicities increase, the Bragg band starts from being convoluted with LSPR (140 – 200 nm), to separated (220 – 320 nm), to producing second order band that's convoluted with LSPR (360 – 400 nm), to second order band separated from LSRP (440 – 480 nm).

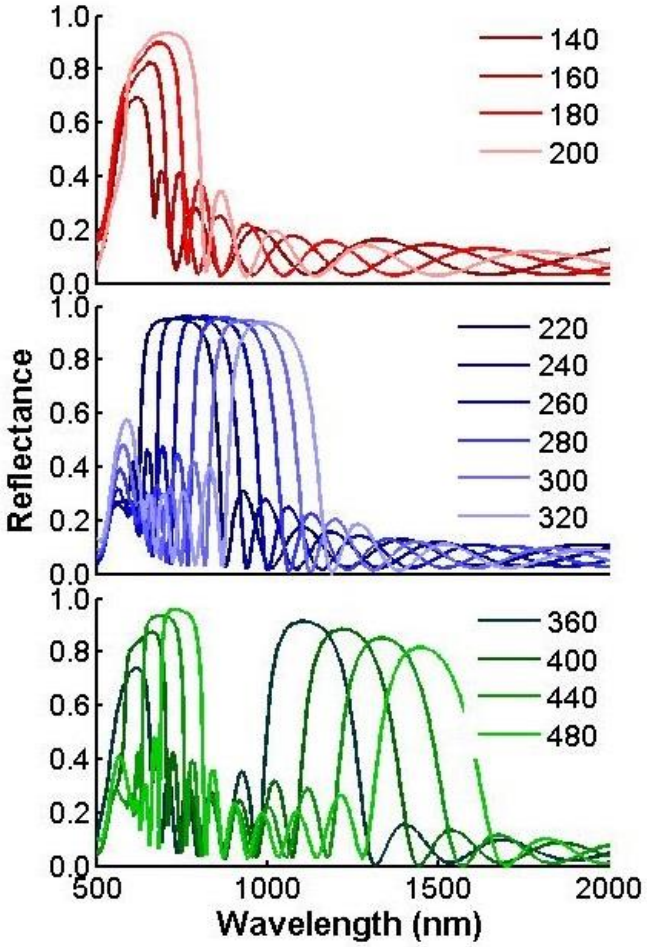

Fig. S12. Dependence on the layer periodicity of the reflectance spectra of tI lattices. The NP radius is 54 nm, and the lattices have 7 layers. Lattice constants in the x-y plane (*a*) is kept at 200 nm. Layer periodicities are shown in the legends. Notice how similar the spectra are compared to the ones in Fig. S11. Similarly, as the layer periodicities increase, the Bragg band starts from being convoluted with LSPR (140 – 200 nm), to separated (220 – 320 nm), to producing second order band that's convoluted with LSPR (360 – 400 nm), to second order band separated from LSRP (440 – 480 nm).

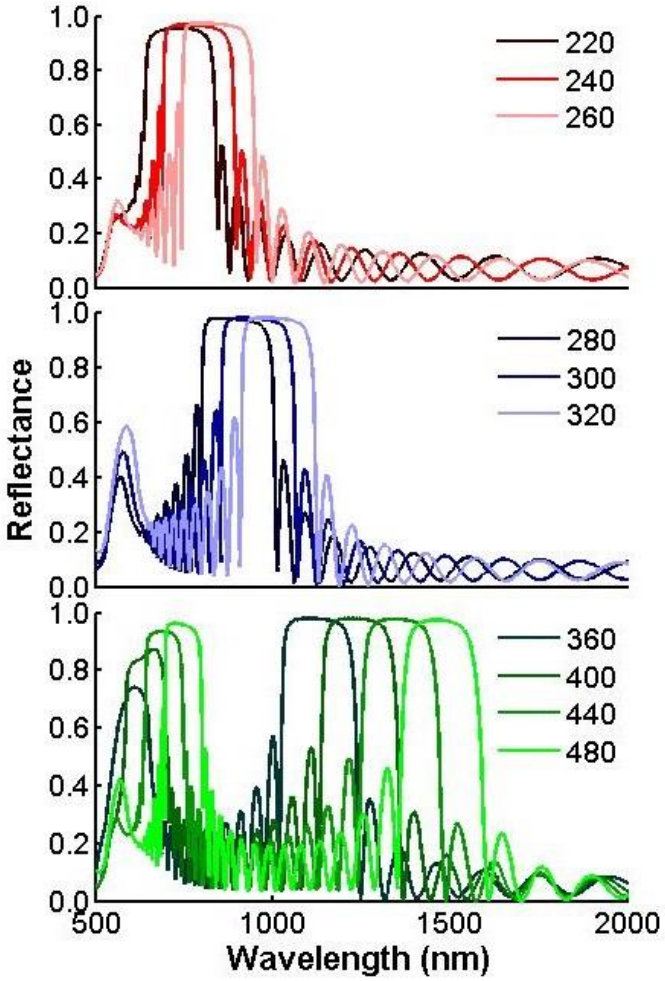

Fig. S13. Dependence on the layer periodicity of the reflectance spectra of tP lattices with 15 layers. The NP radius is 54 nm. This time the lattices have 15 layers. Lattice constant in each metallic layer (*a*) is kept at 200 nm. Layer periodicities are shown in the legends. As the layer periodicities increase, the Bragg band starts from being separated from LSPR (220 – 320 nm), to producing second order band that's convoluted with LSPR (360 – 400 nm), to second order band separated from LSRP (440 – 480 nm).

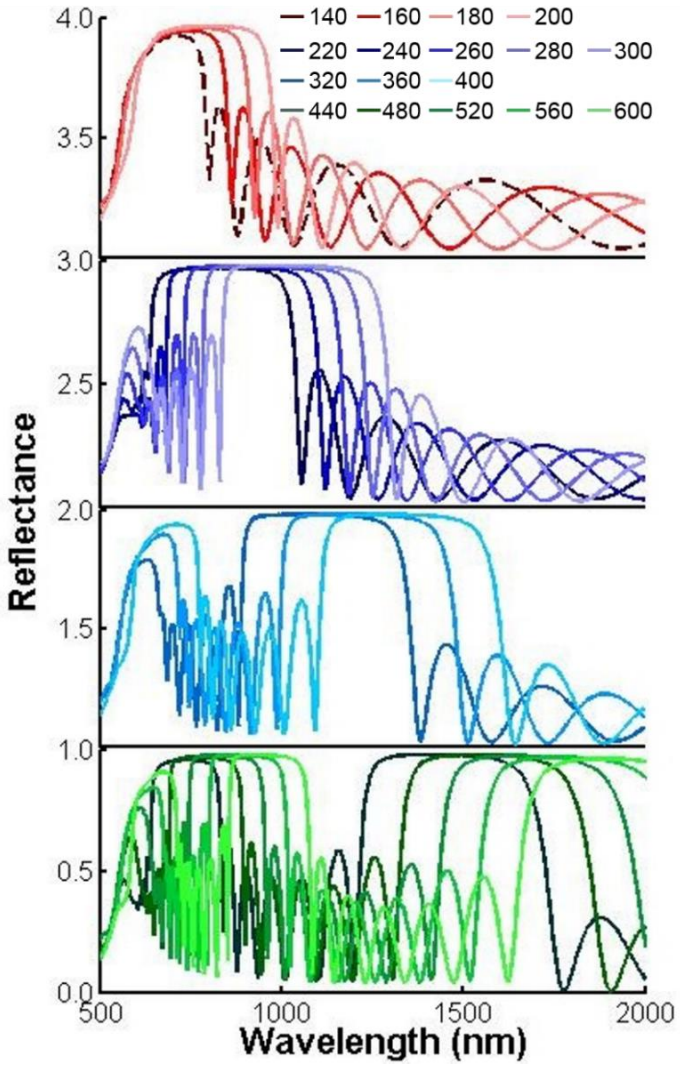

Fig. S14. Dependence on the layer periodicity of the reflectance spectra of tP lattices with a = 140 nm. The NP radius is 54 nm, and the lattices have 7 layers. Lattice constant in the x-y plane (*a*) is kept at 140 nm, which is smaller than that shown in the Fig. S11. Layer periodicities are shown in the legends. In this case, large Bragg reflection band is observed for all layer periodicities investigated. More interestingly, as the layer periodicities increase, the Bragg band starts from being convoluted with LSPR (140 – 200 nm), to separated (220 – 300 nm), to producing second order band that's convoluted with LSPR (320 – 400 nm), to second order band separated from LSRP (440 – 600 nm).

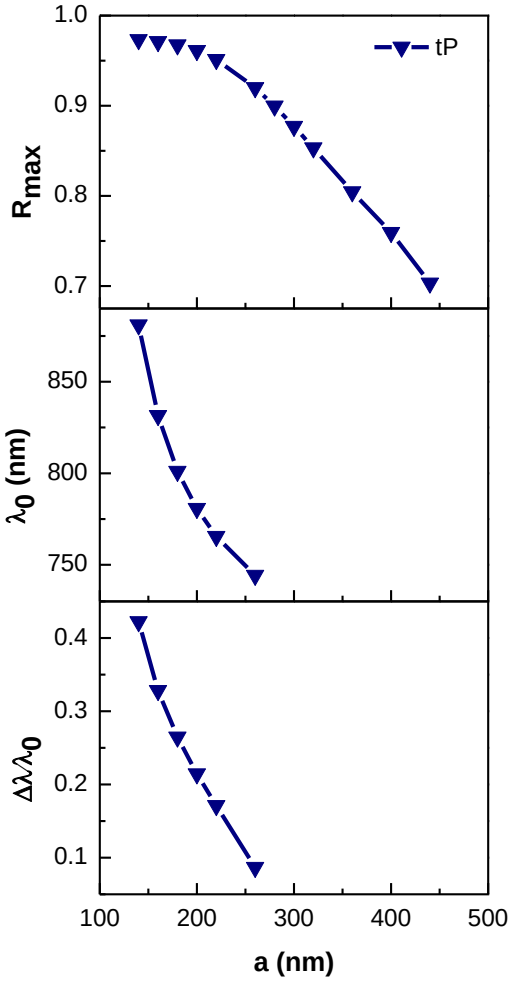

Fig. S15. Dependence of maximum reflectance, λ_0, and $\Delta\lambda/\lambda_0$ on the lattice constant (a) in each layer of tP lattices. The NP radius is 54 nm, and the lattices have 7 layers. Layer periodicity is kept at 240 nm.

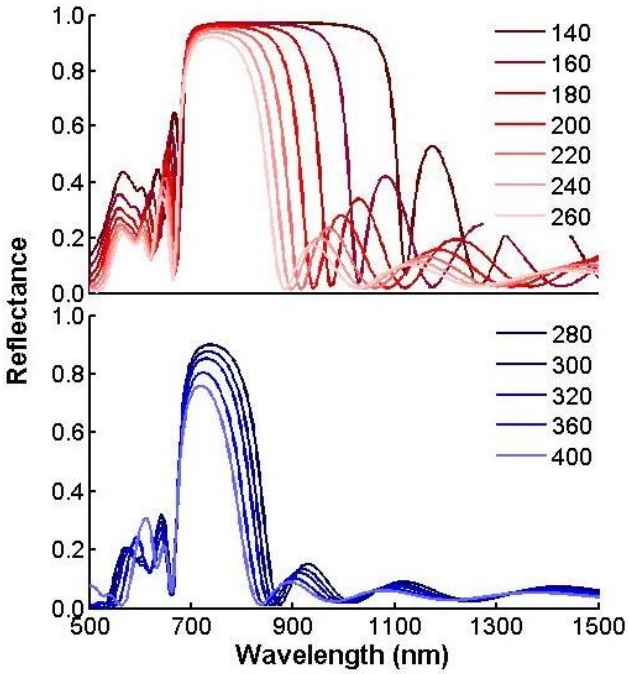

Fig. S16. Dependence of the reflectance spectra on the lattice constant in each layer of tP lattices. The NP radius is 54 nm, and the lattices have 7 layers. Layer periodicity is kept at 240 nm. Lattice constants in each metallic layer are shown in the legends. Interestingly, as the lattice constants in each layer increase, the lower energy side of all the reflection bands seems to be at the same wavelength, while the band width and reflectance on the rest of the band decreases.

5.2 Results of Orthorhombic Superlattices

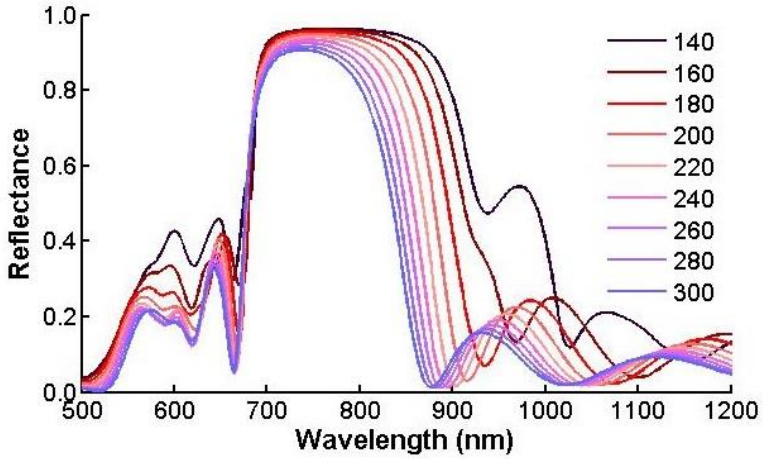

Fig. S17. The reflectance spectra dependence on the lattice constant in each layer of oP lattices. The NP radius is 54 nm, and the lattices have 7 layers. Layer periodicity is kept at 240 nm. One lattice constant in each metallic layer (*a*) is kept constant at 250 nm, while the other (*b*) is shown in the legends. Again, the higher energy side of all the reflection bands seems to be at the same wavelength, while the band width and reflectance on the rest of the band decreases.

5.3 Results of Hexagonal Superlattices

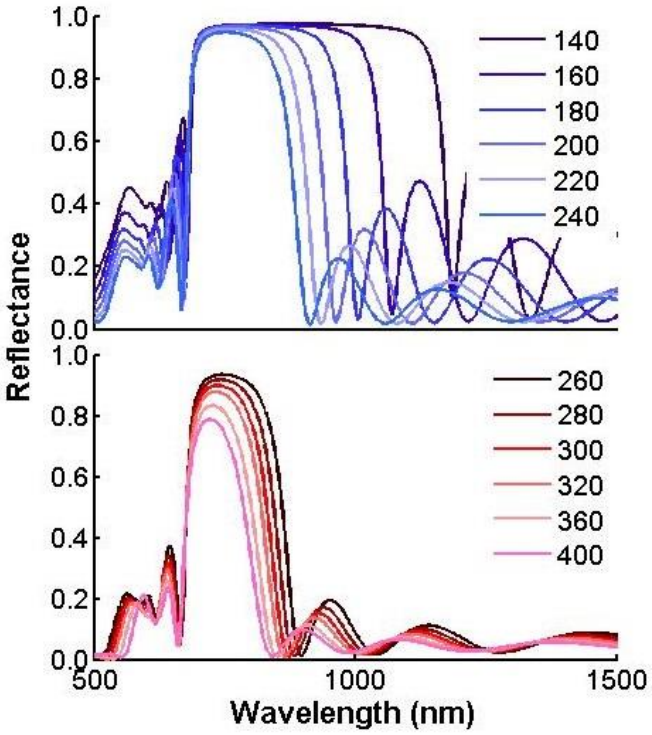

Fig. S18. Dependence on the NP spacing in each layer of the reflectance spectra of hP lattices. The NP radius is 54 nm, and the lattices have 7 layers. Layer periodicity is kept at 240 nm. Lattice constant in each layer is shown in the legends. The higher energy side of all the reflection bands seems to be at the same wavelength, while the band width and reflectance on the rest of the band decreases.

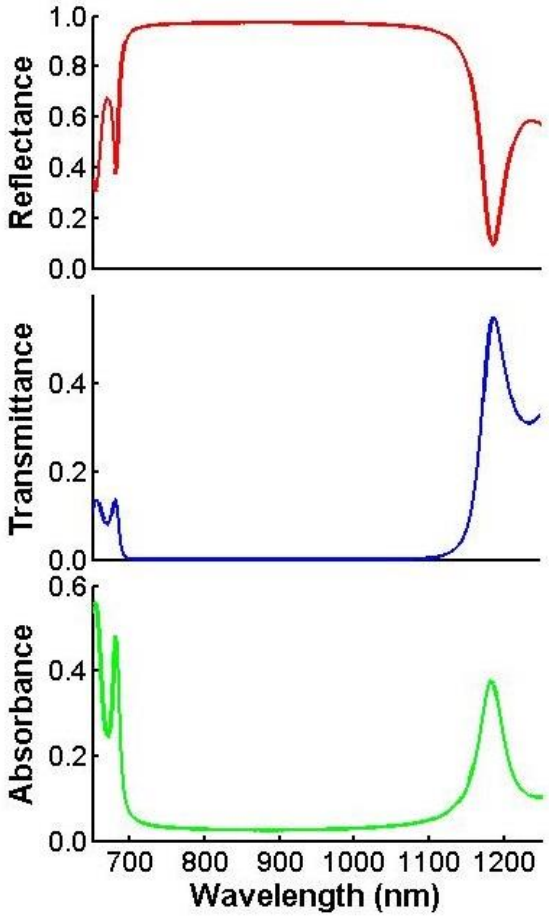

Fig. S19. Reflectance, transmittance and absorbance of a hP lattice. The NP radius is 54 nm, and the lattices have 7 layers. The lattice constant in each layer is 140 nm, and the layer periodicity is 240 nm. This is the same lattice with the largest volume fraction in the previous figure. The highest reflectance is ~97%, due to the material absorption, as can be seen in absorbance spectrum (bottom).

5.4 Results of Trigonal Superlattices

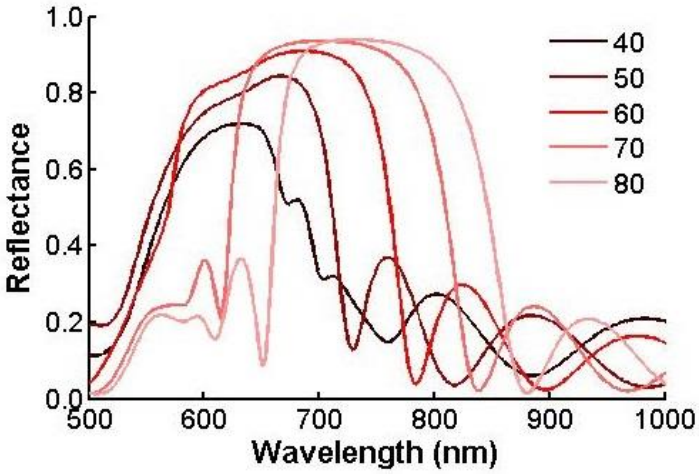

Fig. S20. Dependence on the angle between each layer of the reflectance spectra of hR lattices. The NP radius is 54 nm, and the lattices have 7 layers. Layer periodicity is kept at 240 nm. Lattice constant in each layer is shown in the legend.

5.5 Results of Monoclinic Superlattices

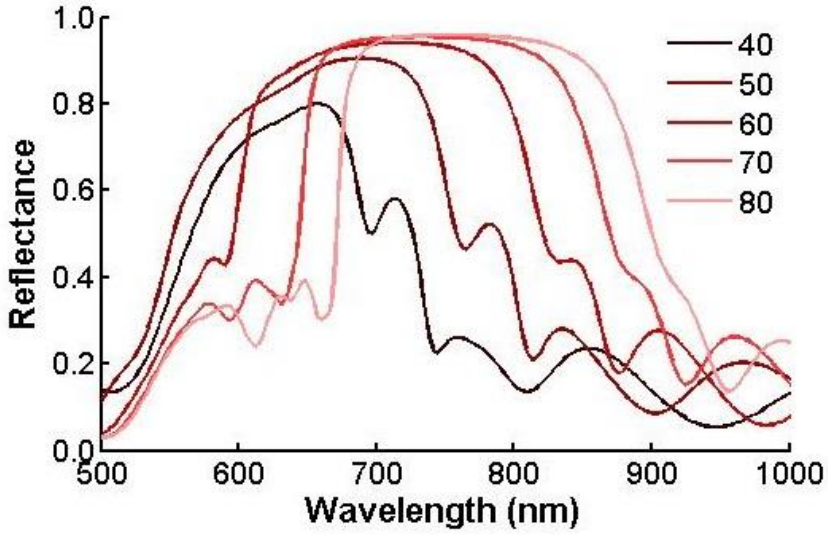

Fig. S21. Dependence on the angle between each layer of the reflectance spectra of mP lattices with fixed c. The NP radius is 54 nm, and the lattices have 7 layers. The three monoclinic lattice constants are kept constant. The angle is shown in the legend.

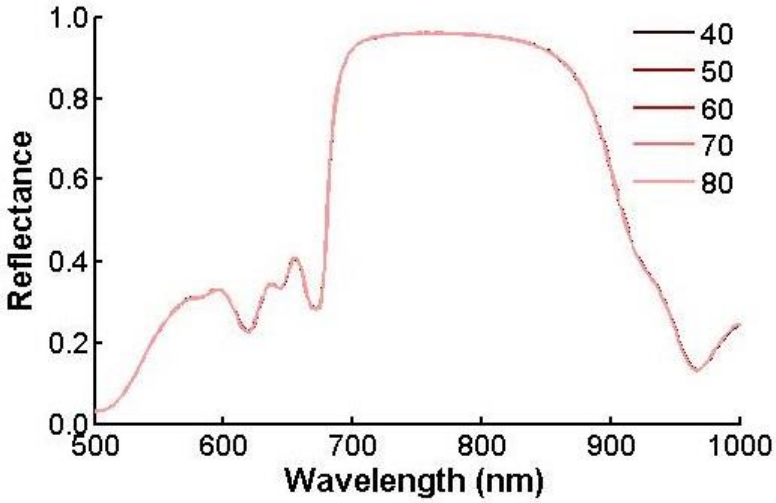

Fig. S22. Dependence on the angle between each layer of the reflectance spectra of mP lattices with fixed z. The NP radius is 54 nm, and the lattices have 7 layers. The lattice constant in each layer and the layer periodicity are kept constant. The angle is shown in the legend. All the spectra are exactly on top of each other.

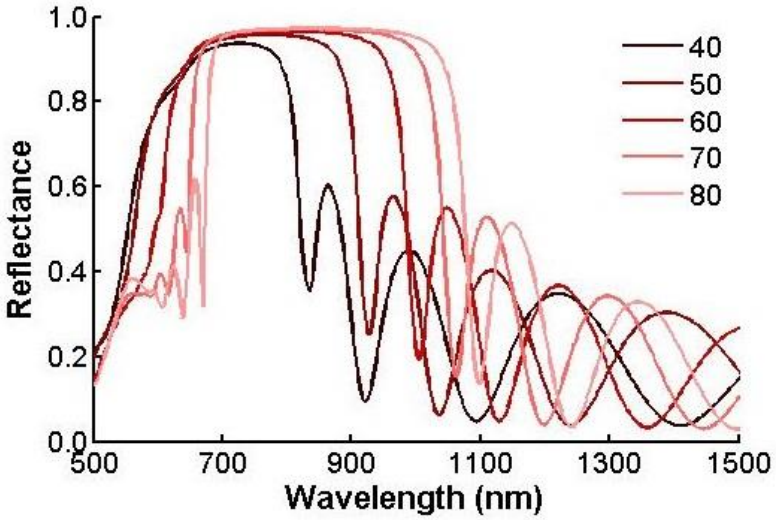

Fig. S23. Dependence on the angle between each layer of the reflectance spectra of mC lattices with fixed c. The NP radius is 54 nm, and the lattices have 7 layers. The three monoclinic lattice constants are kept constant. The angle is shown in the legend. The reflectance of the mC lattices is higher than that of its monoclinic counterpart because of higher volume fraction in each layer.

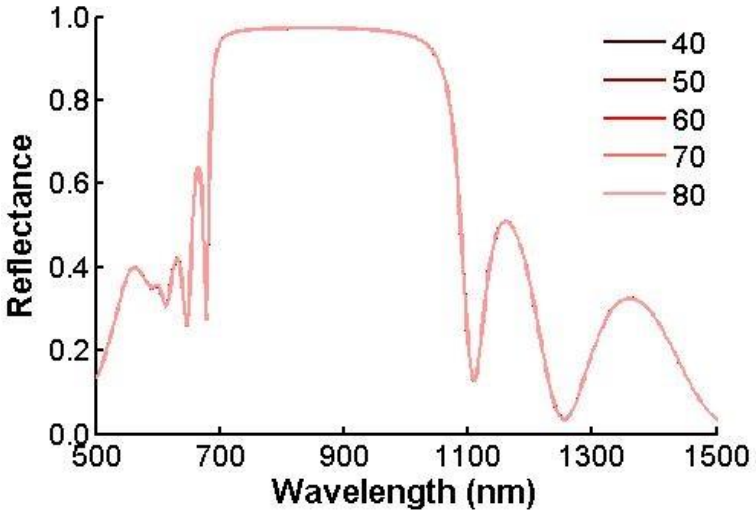

Fig. S24. Dependence on the angle between each layer of the reflectance spectra of mC lattices with fixed z. The NP radius is 54 nm, and the lattices have 7 layers. The lattice constant in each layer and the layer periodicity are kept constant. The angle is shown in the legend. All the spectra are exactly on top of each other. The reflectance of the mC lattices is higher than that of its monoclinic counterpart because of higher volume fraction in each layer.

6. Reflectance with Effective Medium Theory and Transfer Matrix Method

Since the volume fraction, rather than the exact arrangement of the NPs, within each NP layer affects the properties of the stop-band, one can use the Maxwell-Garnett Effective Medium Theory (EMT) (4) to obtain the effective index n_{eff} of the NP layer, followed by using the Transfer Matrix Method (TMM) (19), as commonly used in layered dielectric films, to calculate the reflectance and transmittance of the superlattices. The n_{eff} is only dependent on the dielectric constants of the composite materials and the volume fraction by the equation:

$$\frac{\varepsilon_{eff} - \varepsilon_{matrix}}{\varepsilon_{eff} + 2\varepsilon_{matrix}} = FF * \frac{\varepsilon_{Au} - \varepsilon_{matrix}}{\varepsilon_{Au} + 2\varepsilon_{matrix}} \quad (4)$$

where *FF* is the fill factor (volume fraction of Au) in each layer, as explained in Fig. 3 and Fig. S25. ε_{Au} and ε_{matrix} are the dielectric constant of Au and the background matrix (Au is embedded in silica in this case). The ε_{eff} is the effective dielectric constant of the layer and n_{eff} can then be calculated as the square root of ε_{eff}. The real and imaginary part of the n_{eff} of the NP layers in three simple cubic lattices with 200, 240, and 300 nm lattice constant (*a*) are show in Fig. S25. As can be seen, the smaller the lattice constant (hence larger *FF*), the larger the real part of n_{eff}, which is important since large index contrast is desired.

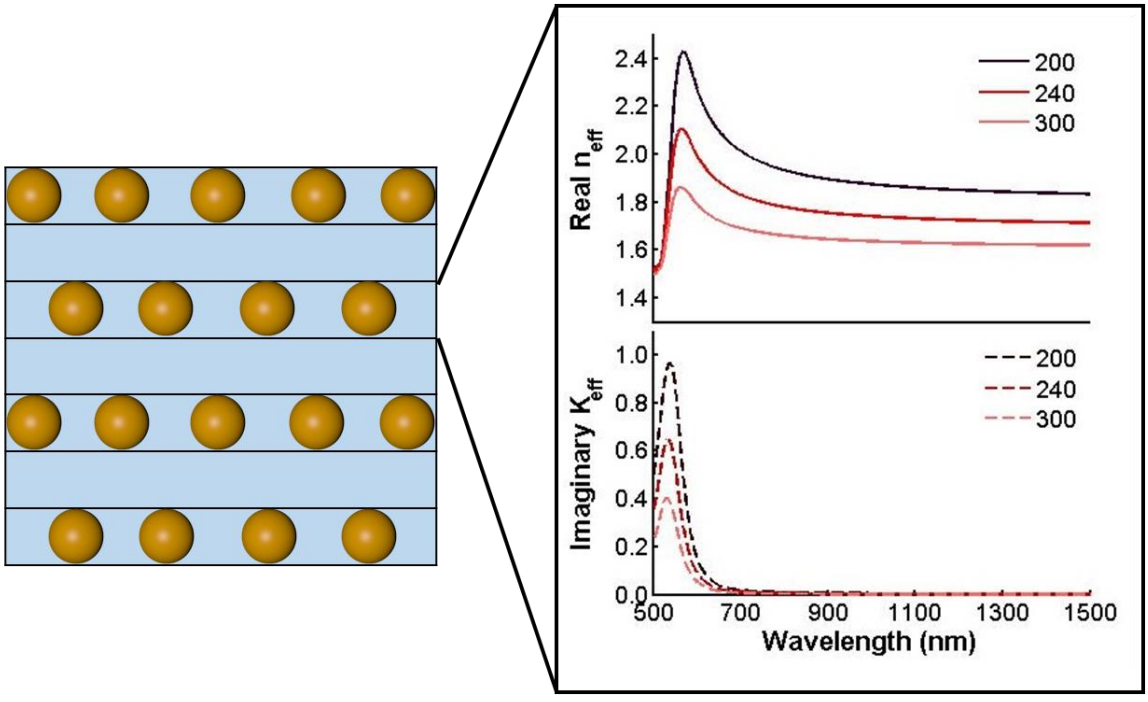

Fig. S25. The real and imaginary part of the effective index calculated with EMT. Here the thickness of the NP layer is twice that of the NP radius. Simple cubic superlattices are used and the lattice constants are shown in the legend.

Now that we know both n_{eff} and n_{si} (1.46), one can calculate the reflectance, transmittance and absorbance of the layered structure by using the TMM. Fig. S26 compares the results calculated through the EMT+TMM codes (done in Matlab) and FDTD of the three superlattices mentioned in the previous paragraph. Overall there is good agreement between the two methods, especially at longer wavelength. The EMT+TMM method underestimates the strength of the stop-band, likely because of blurring of the index contrast. In other words, the full FDTD calculation sees much larger dielectric contrasts. The agreement at shorter wavelength (around or below the NP LSPR at ~600 nm) is poorer mostly due to the limitation in EMT. For example, the quadrupole mode at ~ 550 nm is not predicted by EMT. And when a = 200 nm, the LSPR and stop-band is separate with EMT methods, while the two couple with FDTD.

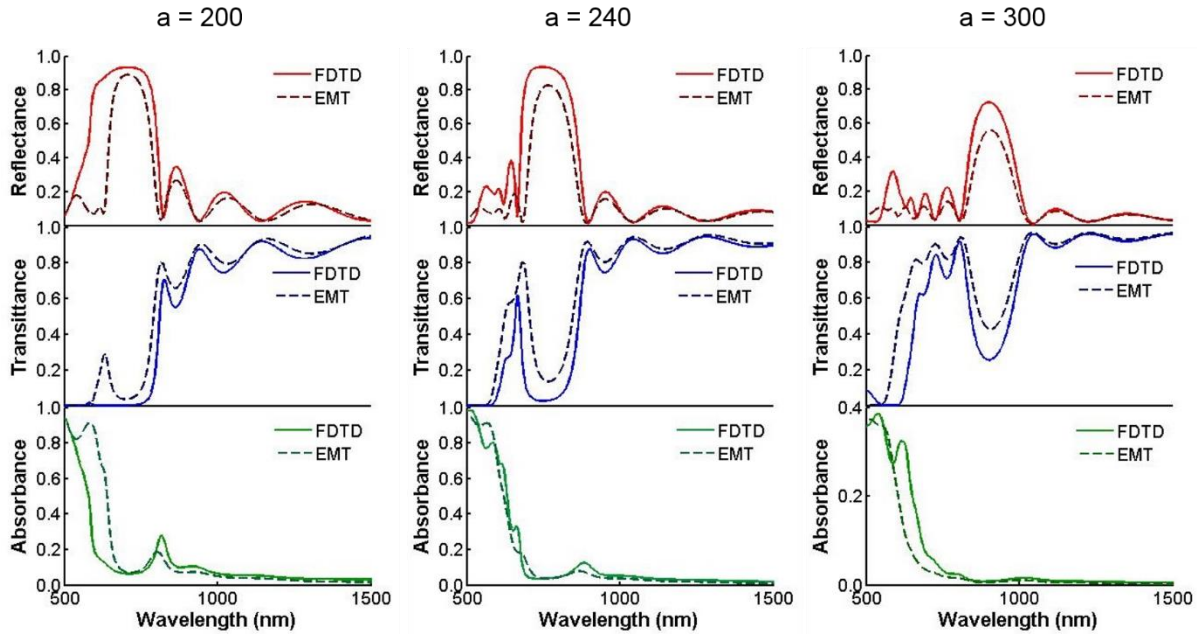

Fig. S26. Comparison between FDTD and EMT methods. Reflectance (top), transmittance (middle) and absorbance (bottom) spectra of simple cubic superlattices with 7 layers and 200 (left), 240 (center) and 300 (right) nm.

7. Angle-Dependent Reflectance Spectra

The dependence of reflectance on the incidence angle is investigated through simulation and plotted in Fig. S27. NPs with 54 nm in radius are arranged in cP lattice with 300 nm lattice constant and 30 layers, in order to ensure sufficient number of layers are used and the reflectance is saturated. The stopband, which is the red-colored broad band in Fig. S27, blue-shifts as the angle of incidence increases. This is because as the angle of incidence increases, the effective layer periodicity along the light propagation direction decreases, thus the stopband shifts shorter wavelength. The stopband exists up until ~ 50° then gradually disappears at steep angle of incidence, due to the fact the distinction between high- and low-index materials become blurred along a certain range of angles.

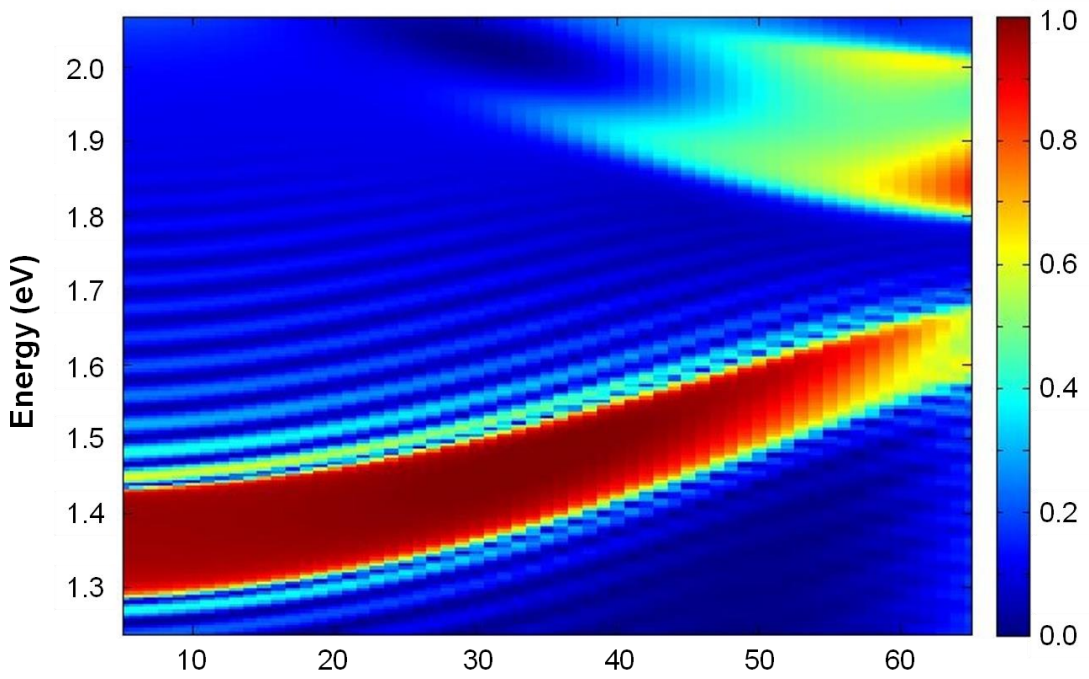

Fig. S27. Angle-dependent reflectance spectra of simple cubic superlattices. The NPs are 54 nm in radius, and the lattice constant is 300 nm. 30 layers are simulated to ensure sufficient layer number. The stopband blue-shifts as the angle of incidence increases, which can be rationalized since the layer periodicity decreases accordingly. At steep angles (> 50°) the definition between the high- and low-index layers along the light propagation becomes blurry, thus the stopband gradually disappears.

8. Effect of Nanoparticle Size

The effect of NP size is explored by using cP lattices with the same densities (i.e. constant volume fractions of the overall superlattice) and 7 layers, we compare the photonic properties of superlattices made with nine different NP sizes (10 – 90 nm in radius) and four volume fractions (8.2%, 10%, 15%, 20%). The lattice constants are summarized in Table S2.

Table S2. Lattice constants in nanometers used for different NP radius (r) and volume fractions (vf) for simple cubic superlattices. Lattice constants are in nm.

r(nm) / vf (%)	10	20	30	40	50	60	70	80	90
8.2	37	74	111	148	185	222	259	296	333
10	35	69	104	139	174	208	243	278	313
15	30	61	91	121	152	182	212	243	273
20	28	55	83	110	138	165	193	220	248

No reflectance larger than 0.9 is observed in 10-40 nm NP superlattices at all six volume fractions (Fig. S28). For superlattices with 50-90 nm NPs, R_{max} increases to a saturation value (Fig. S30*B*). Moreover, the larger the NP size, the more the stopband is to the red, which is true for all volume fractions (Figs. S29 and S30*C*). This is likely because that at a constant volume fraction, the layer periodicity is larger for larger NP size, thus λ_0 increases as predicted by equation (4). Likewise, the stopband blue shifts as the volume fraction increases, due to smaller layer periodicity at larger volume fraction. From Fig. S30 we see that at sufficient volume fraction both the R_{max} and $\Delta\lambda/\lambda_0$ increases with larger NPs. Thus, at a constant Au volume fraction, larger NPs are more suitable for optimizing PPCs performance.

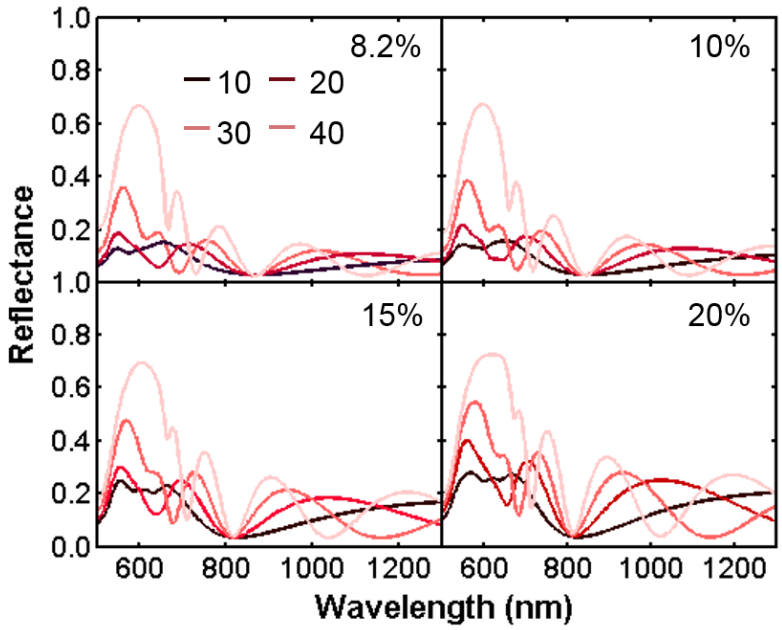

Fig. S28. Reflectance spectra of simple cubic superlattices with small NP building blocks at four volume fractions. The NP size is indicated in the legend, and the volume fraction is shown in the top-right corner of each plot. The lattices have 7 layers. No reflectance larger than 0.9 exists when the three sizes of NPs are used at all four volume fractions.

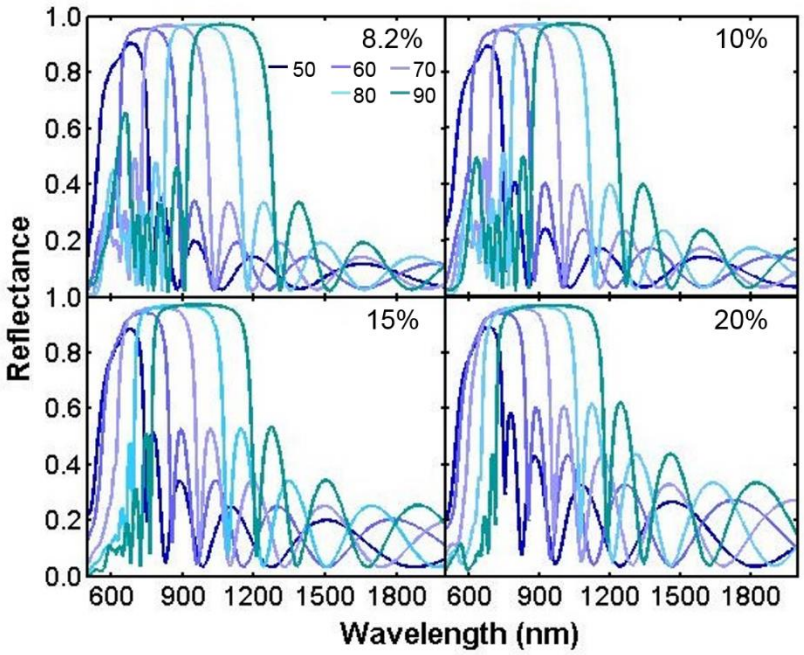

Fig. S29. Reflectance spectra of simple cubic superlattice with larger NP building blocks at four volume fractions. The NP size is indicated in the legend, and the volume fraction is shown in the top-right corner of each plot. The lattices have 7 layers. As is evident, the stop-band becomes broader with larger NP building blocks.

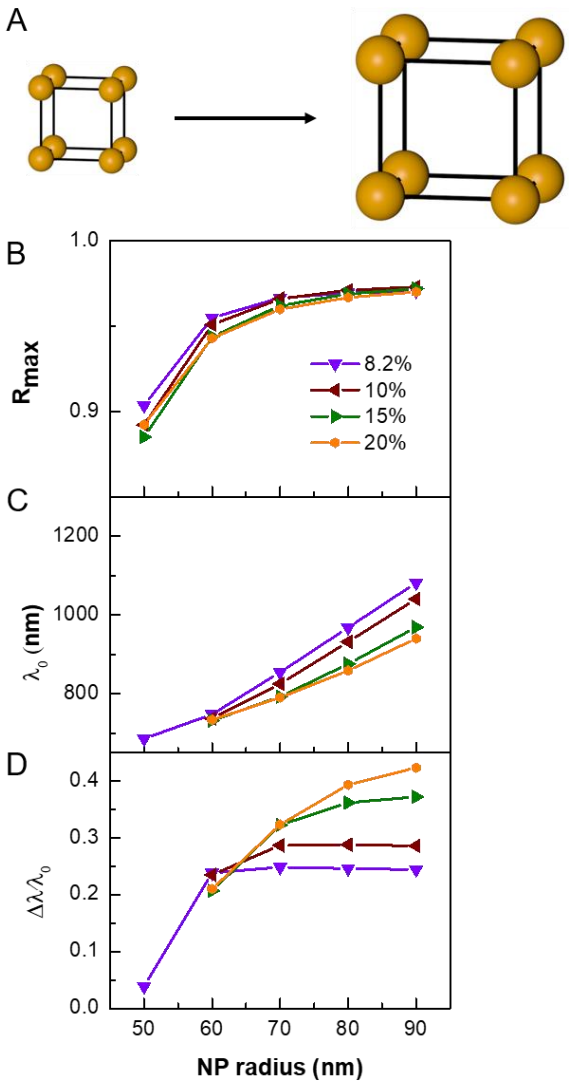

Fig. S30. NP size as a design parameter for PPCs. (*A*) At the same volume fraction and lattice symmetry (simple cubic), the effect of the NP size on the stopband features is explored. (*B-D*) The dependence of R_{max} (*B*), λ_0 (*C*) and $\Delta\lambda/\lambda_0$ (*D*) on NP size of four different volume fractions as shown in the legend.

9. Bandstructure of PPCs

The stop-band that is observed in the reflectance spectra can also be viewed in the band diagram of the corresponding superlattice. To avoid interband transitions in Au, the Drude model is used to generate the dielectric constant of Au:

$$\varepsilon_D(\omega) = \varepsilon_\infty - \frac{\omega_D^2}{\omega^2 + i\gamma_D\omega} \tag{5}$$

where ε_∞ = 11.4577, ω_D = 9.4027 eV, and γ_D = 0.08314 eV. The calculated refractive index is compared with the experimental results from Johnson and Christy in Fig. S31.

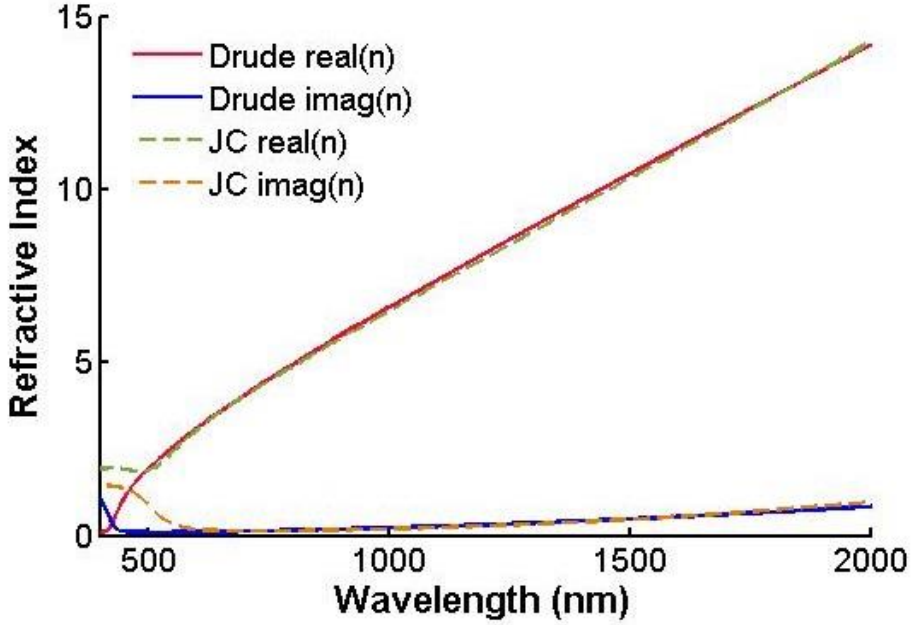

Fig. S31. Comparison between the refractive indexes obtained from Drude model and experimental results. The real ("Drude real(n)") and imaginary ("Drude imag(n)") part of the refractive index from the Drude model fits well with the real ("JC real(n)") and imaginary ("JC imag(n)") part of the experimental results reported by Johnson and Christy (1).

By importing the Drude model as the material property, a single simple cubic unit cell of spherical gold NP with 54 nm radius is simulated. Bloch boundary conditions are used in all three dimensions and the dispersion relation in the ΓX direction is investigated. The unit cell is excited with multiple randomly distributed dipole sources. The electric field as a function of time is collected by multiple randomly placed monitors and Fourier-transformed to produce the dispersion relation (Fig. S32).

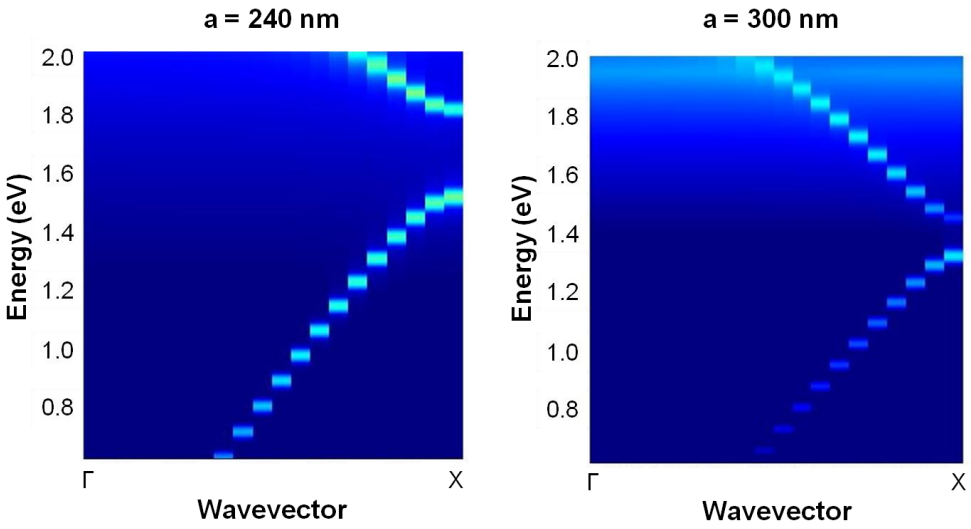

Fig. S32. Band diagram of simple cubic lattice with two different lattice constants. The lattice constants are labeled on top of the band diagram.

Large Ag NPs with larger lattice constant are also investigated in order to separate the photonic band gap from the NP LSPR. Fig. S33 shows the bandstructure of a cP lattice with 180 nm NP and 300 nm lattice constant. A broad bandgap exists in the ΓX direction but gradually closes up in other directions. This shows a similar trend to our angle-dependent study shown in Fig. S27. A full photonic band gap is observed in a diamond lattice, as can be seen in the case of a diamond lattice made of 180 nm Ag NPs and 500 nm lattice constant, in order to avoid NP touching (Fig. S34). The band gap is 0.42 eV, which is larger than similar structures made with the same volume fraction of high-indexed dielectric materials, as reported by Ho *et al*. (20).

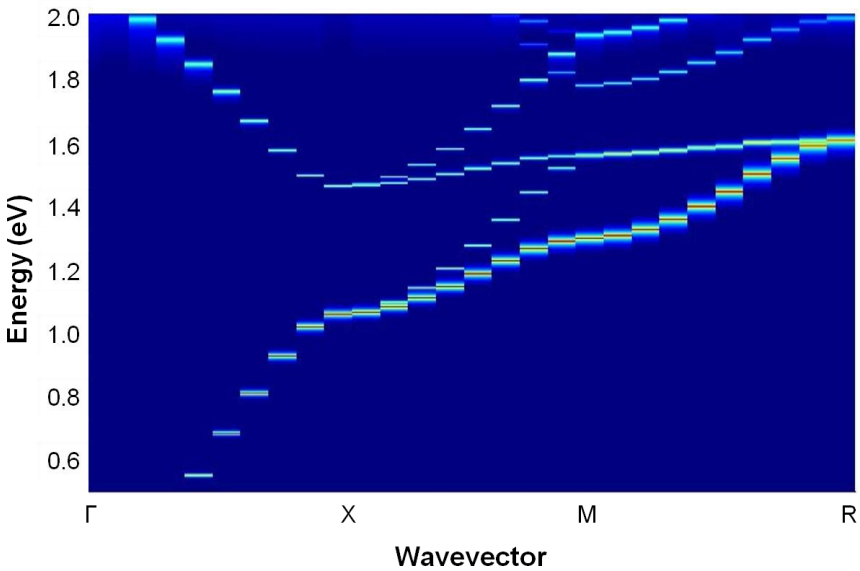

Fig. S33. Band diagram of simple cubic lattice made of Ag NPs. The NPs are 90 nm in radius and the lattice constant is 300 nm.

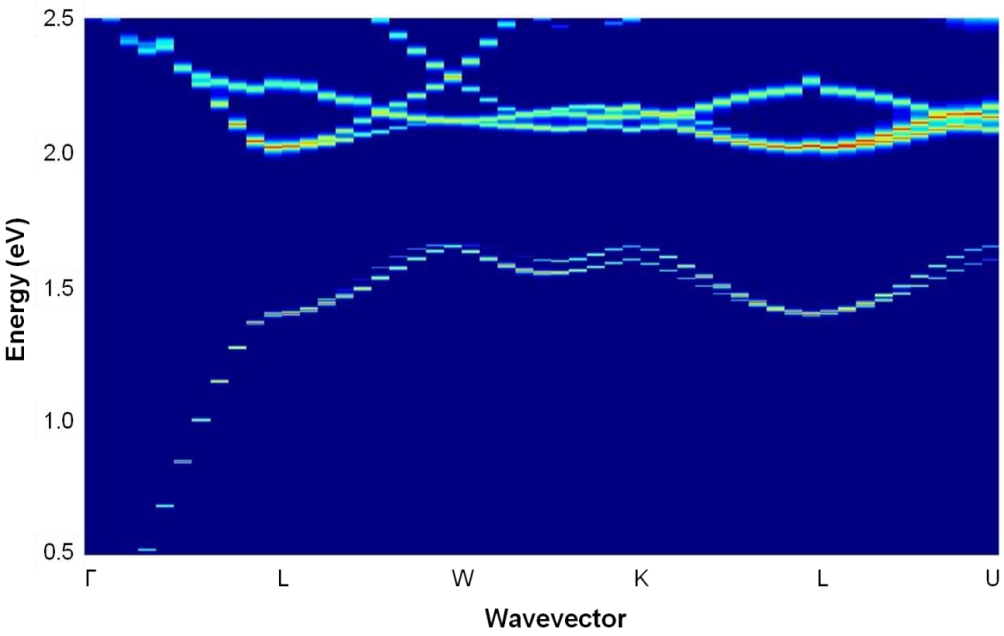

Fig. S34. Band diagram of diamond lattice made of Ag NPs. The NPs are 90 nm in radius and the lattice constant is 500 nm.

.

10. Effect of NP Shape

In order to investigate the effect of NP shape through simulation, spherical, cubic and octahedral NPs of the same volume are used as building blocks. The radius of the spherical NP is 54 nm, the edge length and rounding are 88 and 5 nm for cubic NP and 112 and 5 nm for octahedral NP. Simple cubic lattice structure with 200 nm lattice constant is used such that all the superlattices with different NP shape share the same volume fraction too. Once again, 7 layers are used in the calculations. Fig. S35 shows the reflectance spectra of the three superlattices. Here, we see that the stop-band exists in all three spectra, which indicates that the same general guidelines that are discussed in the main text can be applied to other NP shapes.

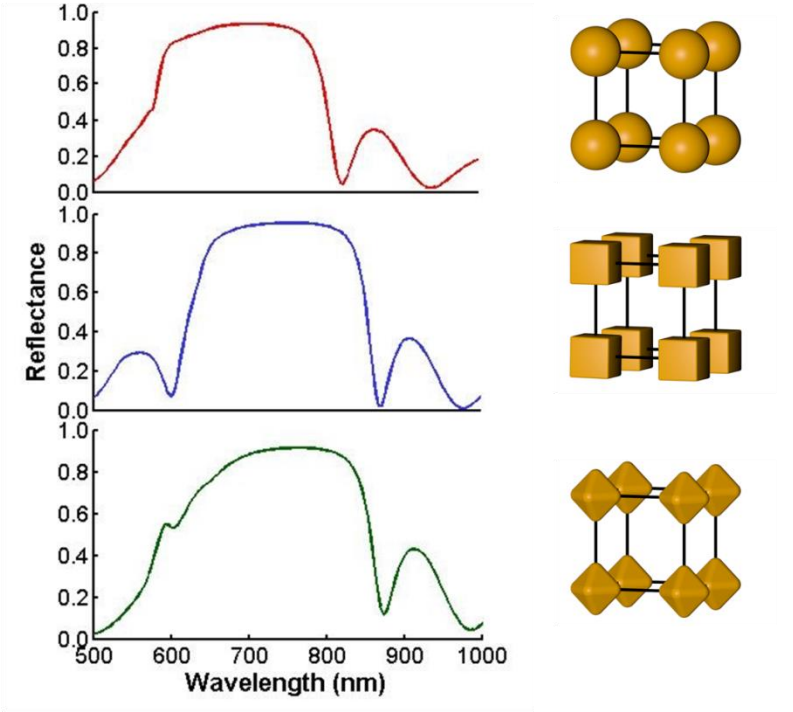

Fig. S35. Reflectance spectra of simple cubic superlattice with spherical (top), cubic (middle) and octahedral (bottom) NPs. The three types of NP building blocks have the same volume and their corresponding superlattices have the same lattice constant and volume fraction. A stop-band is observed in all spectra.

11. Performance of PPCs with Different NP Composition

Here, we perform a set of simulations on superlattices with the same geometry as the experimental sample, namely a simple cubic lattice structure, 134 nm lattice constant, 88 nm cubic NP with 5 nm rounding, but different materials (Ag, Au, Al, Cu). Again, only 7 layers are probed. Fig. S36 shows the reflectance, transmittance and absorbance spectra. Obviously, the stopband of Ag shows the highest reflectance and lowest absorption, followed by Au, Cu and lastly Al. We note that this trend might not hold true in superlattice with different lattice parameters, due to reasons such as the fact that material loss is dependent on the NP size and its dielectric environment and the effective indices depend on wavelength. The highest reflectance of the Ag NP superlattices reaches ~0.986 and might be further increased by adjusting the lattice parameters and layer number. Indeed, the simulated spectra of a tetragonal Ag NP superlattice with 134 nm in-plane lattice constant, 300 nm layer periodicity and 15 layers are plotted in Fig. S37, in which the largest reflectance reaches more than 0.996.

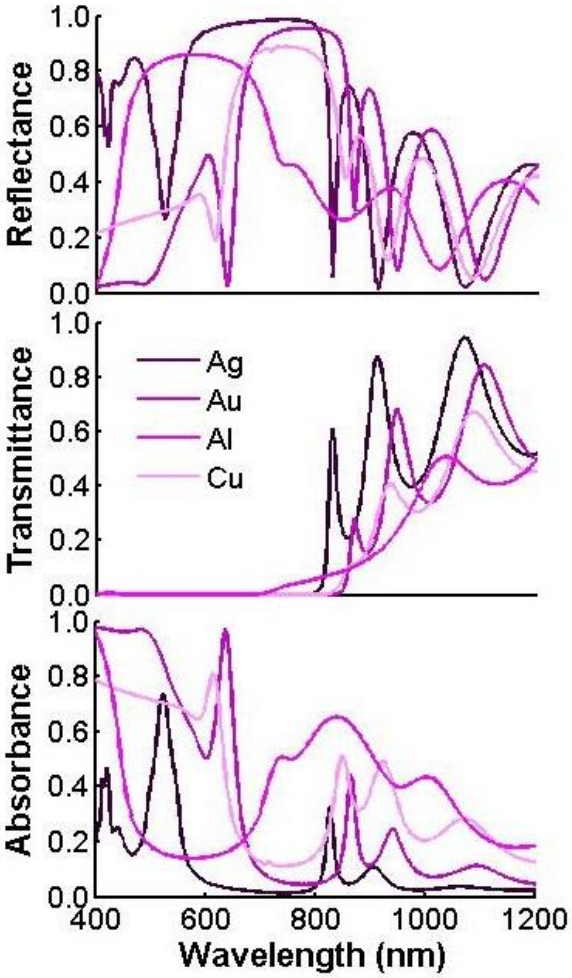

Fig. S36. Reflectance (top), transmittance (middle) and absorbance (bottom) spectra of simple cubic superlattice with Ag, Au, Al, and Cu NPs. Ag NP superlattice shows the largest reflectance and lowest loss at its stop-band wavelengths. The lattice constant is kept at 134 nm, and the number of layers is 7. Cubic NPs with 88 nm edge length and 5 nm rounding are used.

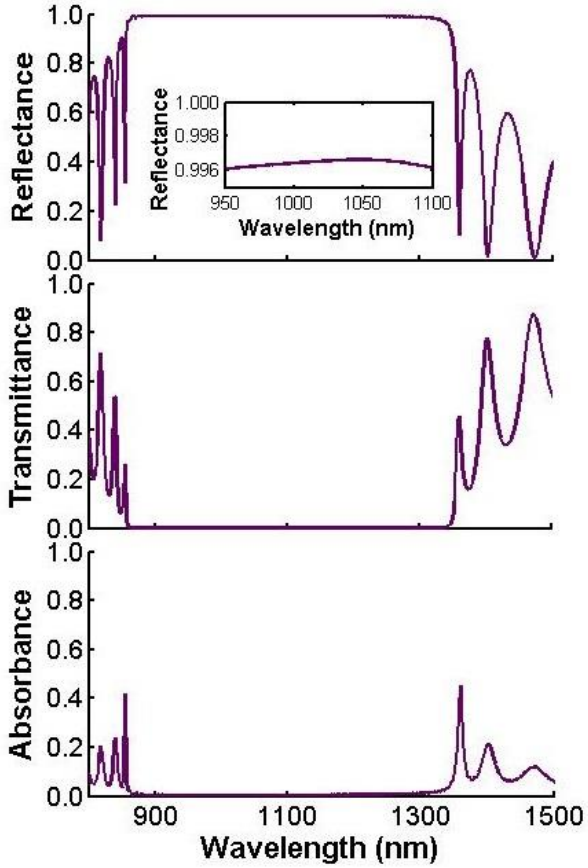

Fig. S37. Reflectance (top), transmittance (middle) and absorbance (bottom) spectra of tetragonal superlattice with Ag NPs. The R_{max} for this structure is ~ 0.996. The structural parameters for this superlattice are a = 140 nm, c = 300 nm, 15 layers. Cubic NPs with 88 nm edge length and 5 nm rounding are used.

12. Performance of PCs with Different Metallic NPs

Here, FDTD simulations where spherical NPs with a 54 nm radius were arranged in a cP superlattice with 134 nm lattice constant were performed. The top part of Fig. S38 summarizes the reflectance spectra of plasmonic NPs (Ag, Au, Al, Cu), where there is a significant stopband, which is absent for lattices made from non-plasmonic NPs (Cr, Fe, Ti, Fig. S38). Further investigation of Ti NP superlattices as a function of changing layer number (Fig. S39) and lattice constant (Fig. S40) reveals that there is not a significant stopband at smaller lattice constants, whereas at larger lattice constants, the stopband is much weaker than the analogous case with plasmonic particles (compare with Fig. S7).

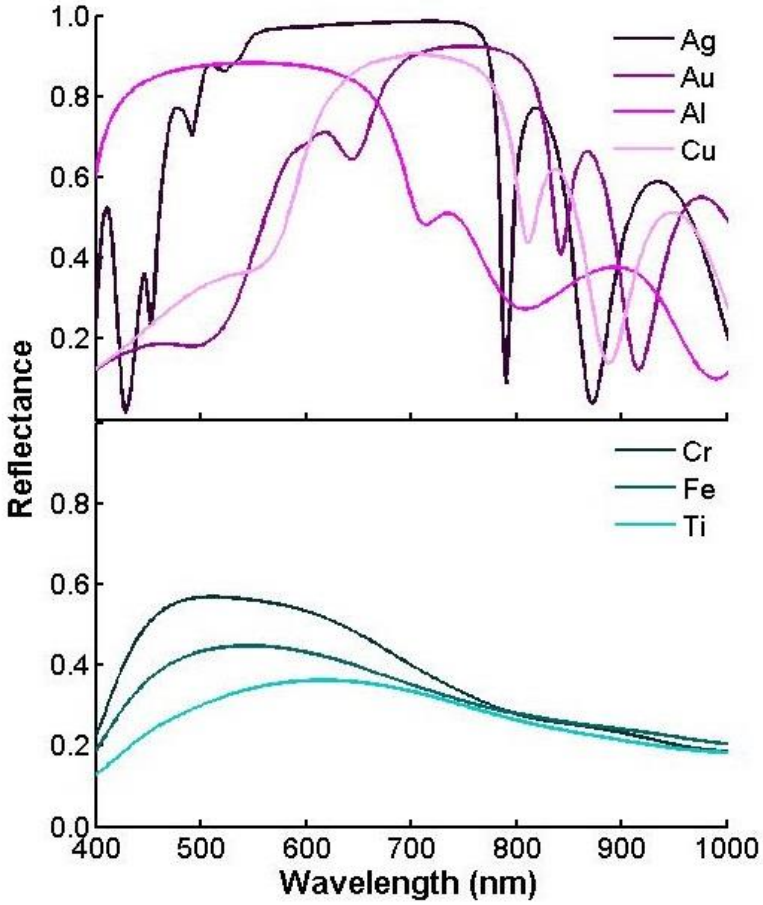

Fig. S38. Reflectance spectra of a simple cubic superlattices with different NP compositions. Plasmonic NPs show large stopband (top) compared to metallic NPs with poor plasmonic properties (bottom). Spherical NPs with 54 nm radius were used, and the lattice constant is 134 nm. 7 layers were used.

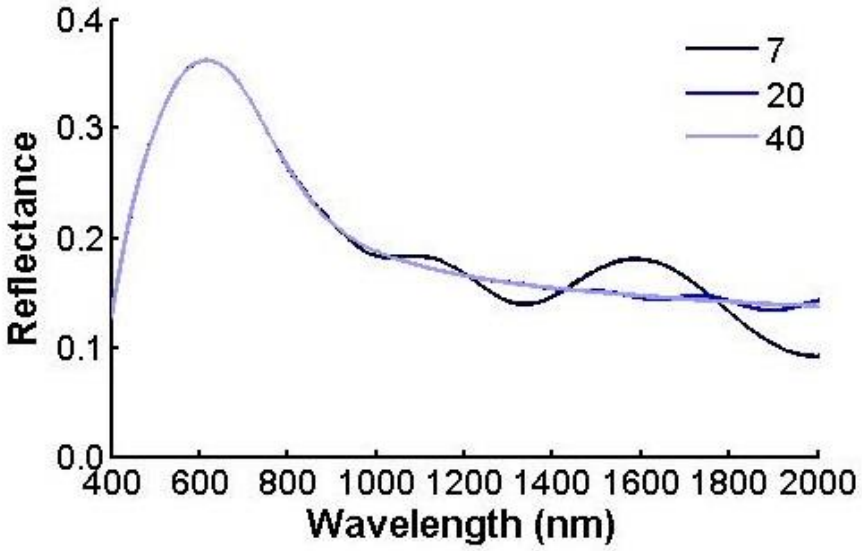

Fig. S39. Thickness dependence of the reflectance spectra. The spherical NPs are made of Ti and the radius is 54 nm, and the crystal has cP symmetry and a 134 nm lattice constant. The number of layers is shown in the legend. The peak at ~600 nm does not change with increasing number of layers (shown in legend).

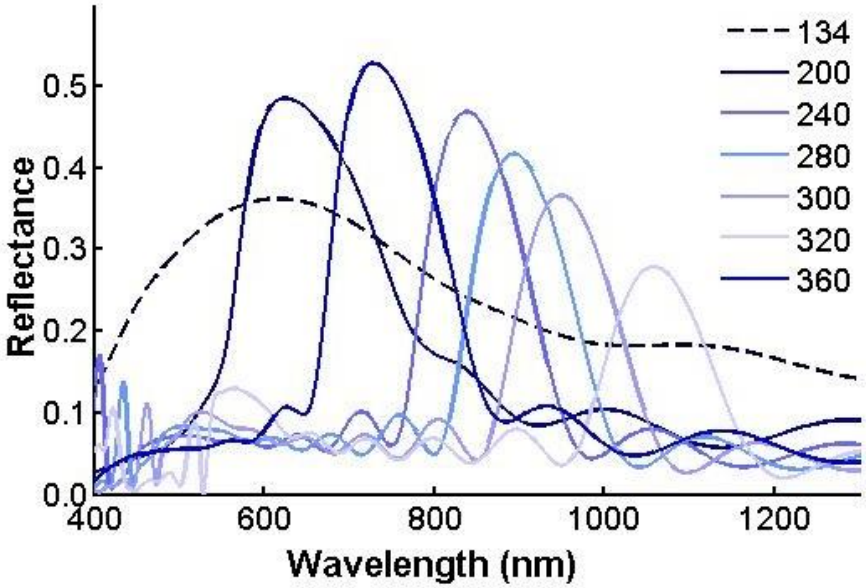

Fig. S40. The reflectance spectra dependence on lattice constant for cP lattices. The NPs are made of Ti, the particle radius is 54 nm, and the lattices have 7 layers. Lattice constants are shown in the legends.

13. Performance of PC with Dielectric NPs

In order to benchmark our technique with conventional PC fabrication methods, simulations are done with dielectric NP building blocks. Specifically, the NPs have 54 nm radius and their material is set to be dielectric with a constant positive refractive index. The NPs are arranged into lattice structures in the same manner as the metallic NP superlattices discussed in the main text. The dielectric NP superlattices show similar behavior as its metallic counterpart, such as a stronger stopband with larger number of layers (Fig. S41), a red-shift as the lattice constant increase (Fig. S42). They also obey well the design principles derived with metallic NP superlattices (Figs. S44-46). Importantly however, a larger number of layers are needed for the stopband to saturate, and the bandwidth is smaller in the dielectric NP superlattice compared to the metallic.

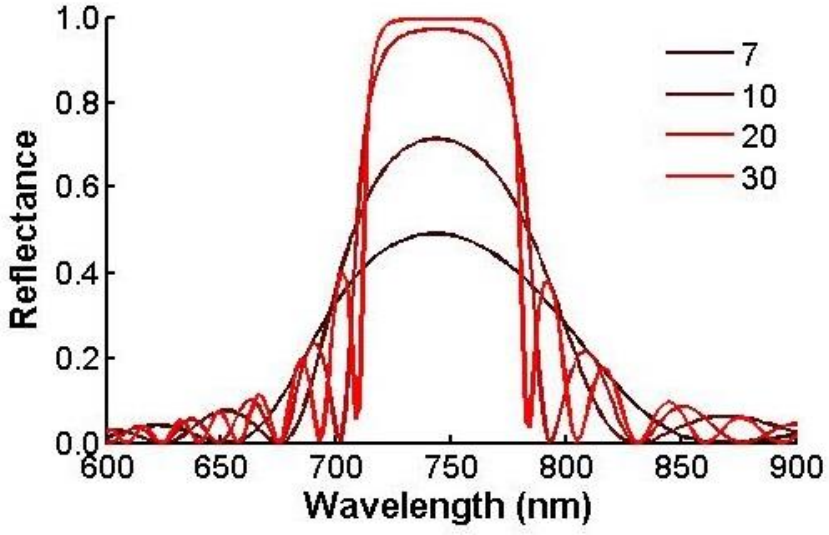

Fig. S41. Thickness dependence of the reflectance spectra of dielectric NP superlattices. The NP radius is 54 nm, the crystal has simple cubic symmetry and 240 nm lattice constant. The number of layers is shown in the legend. The dielectric index of the NPs is fixed at 4. The reflection spectra resemble that of superlattices made with metallic NPs with the exact same lattice parameters. A larger number of layers is required to achieve high reflectance (> 0.9), and the stopband does not saturate even for 30 layers.

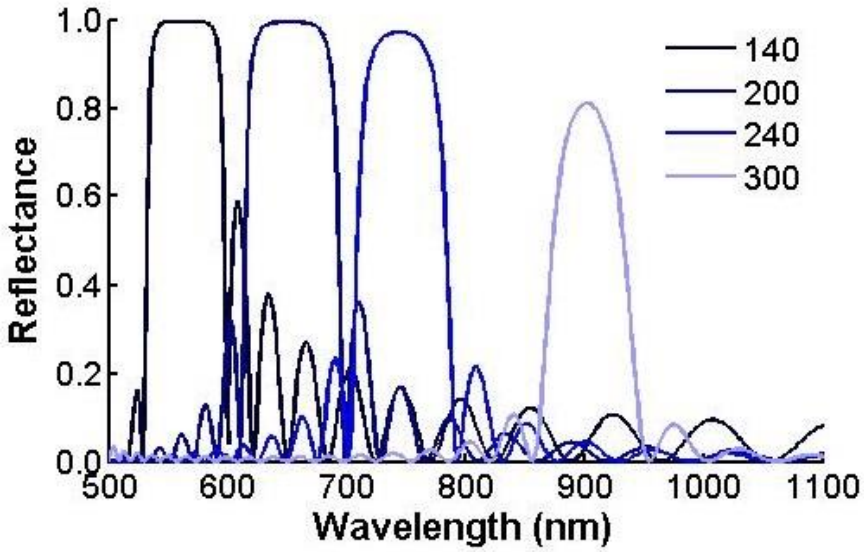

Fig. S42. Dependence on the lattice constant of the reflectance spectra of dielectric NP superlattices. The NP radius is 54 nm, and the crystal has simple cubic symmetry. The number of layers is fixed at 20. The dielectric constant of the NPs is 4. The lattice constant is shown in the legend. The stopband red shifts as the lattice constant increases, similar to the case of plasmonic nanoparticle superlattice.

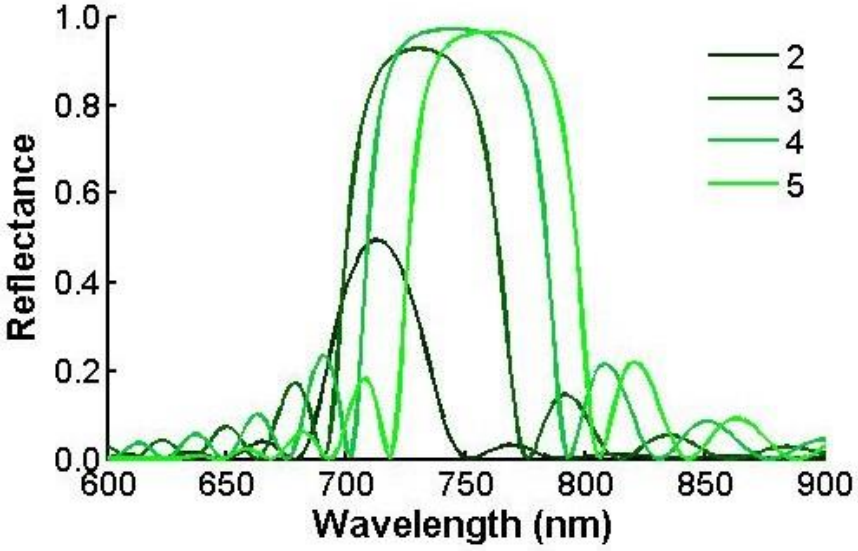

Fig. S43. Dependence on the dielectric index of the reflectance spectra of dielectric NP superlattices. The NP radius is 54 nm, and the crystal has simple cubic symmetry and 240 nm lattice constant. The number of layers is fixed at 20. The dielectric index of the nanoparticles is shown in the legend. As the index increase, there is a slight red-shift in the stopband location.

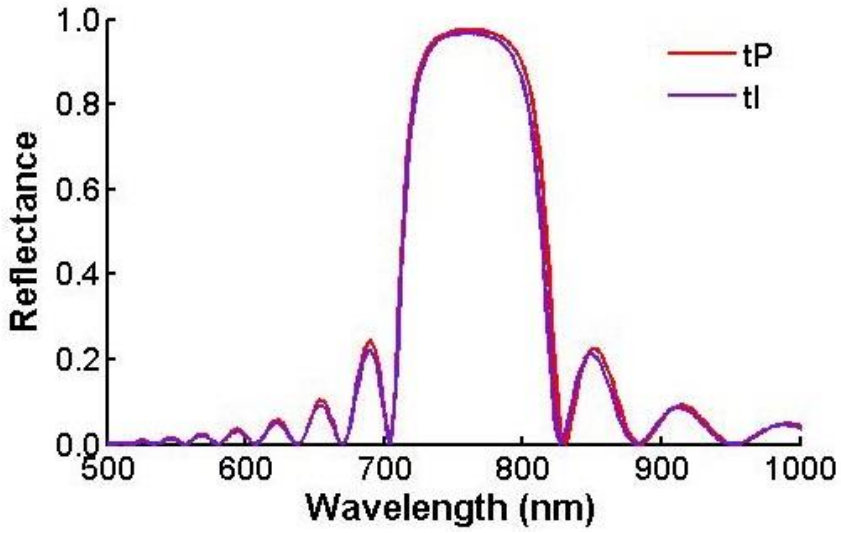

Fig. S44. Effect of layer periodicity on the reflectance spectra of dielectric NP superlattices. The NP radius is 54 nm, and the dielectric constant is 4. The superlattice has 200 nm in-plane lattice constant and 15 layers. The lattice symmetry is shown in the legend. The two spectra coincides with each other well, indicating again that layer periodicity, rather than lattice constant in z-direction, determines the stopband features.

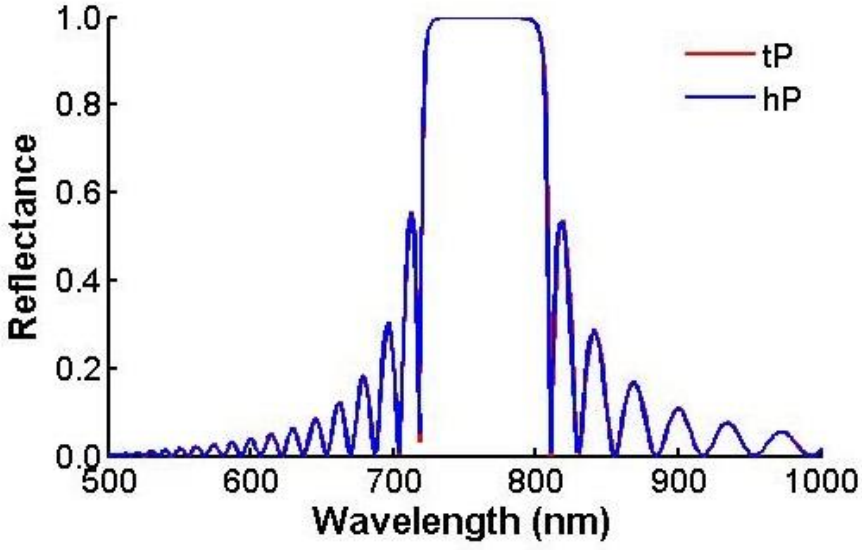

Fig. S45. Effect of NP arrangement in each layer on the reflectance spectra of dielectric NP superlattices. The NP radius is 54 nm, and the dielectric constant is 4. The superlattice has 240 nm layer periodicity and 20 layers. The lattice symmetry is shown in the legend. The two spectra overlap with each other, indicating again that the exact arrangement of nanoparticles in each layer does not affect the stopband features.

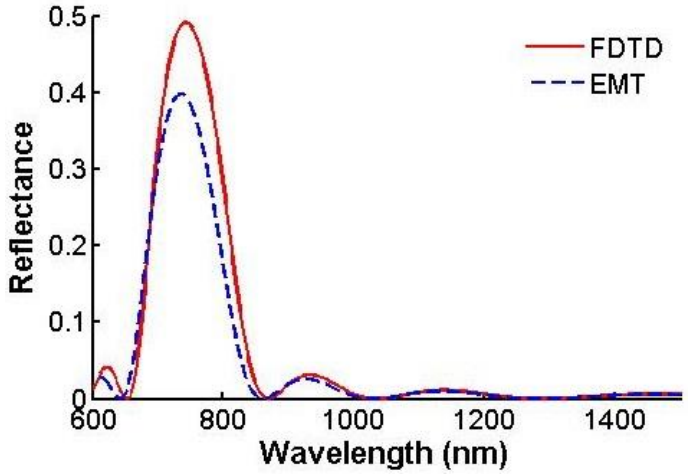

Fig. S46. Comparison between reflectance spectra from FDTD and EMT+TMM methods. The EMT+TMM method is done in the exact same manner as described in section 5 of this SI, except that the inclusion material is dielectric instead of Au. The NP radius is 54 nm and its dielectric constant is 4. The superlattice has simple cubic lattice symmetry, 240 nm lattice constant and 7 layers. Consequently, volume fraction in the NP layer is ~ 21.2% and resulting refractive index of the layer is ~ 1.8 (independent of wavelength). Again, the EMT+TMM method predicts correctly the location of the stopband but underestimates its intensity, just as in the case of lattices made of metallic NP.

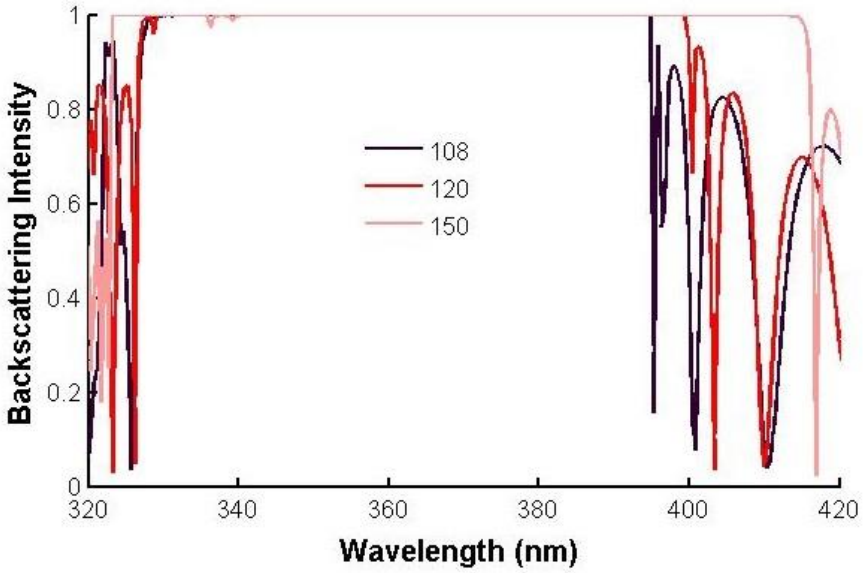

Fig. S47. The stopband features can be improved by the use of spacer group. Dielectric NPs are also used to demonstrate the importance of having spacer groups (i.e. having NPs well-separated). The superlattice has tetragonal symmetry with a = 140 nm and 7 layers. The radius and dielectric constant of the NPs are 54 nm and 4, respectively. The lattice constant in the z direction (c) is shown in the legend. When c = 108 nm, adjacent NP layers are touching. The bandwidth increases as the NP layers are further separated.

14. Effect of Dielectric Medium

The superlattice can have a different dielectric medium. Experimentally, this can be easily achieved by immersing the superlattices in different index-matching oils. Thus, we investigate through simulation the effect of a different dielectric medium. Again, the superlattice is set to have the same structural properties with 88 nm edge length and 5 nm rounding Au nanocubes, simple cubic lattice structure, 134 nm lattice constants and 7 layers. Fig. S48 summarizes the reflectance, transmittance and absorbance spectra of the superlattices with different dielectric medium. Obviously, the spectral location of the stop-band can be easily tuned by changing the dielectric medium. Moreover, the larger the dielectric medium, the broader the stop-band, which might be due to larger index contrast between the metal and dielectric layer.

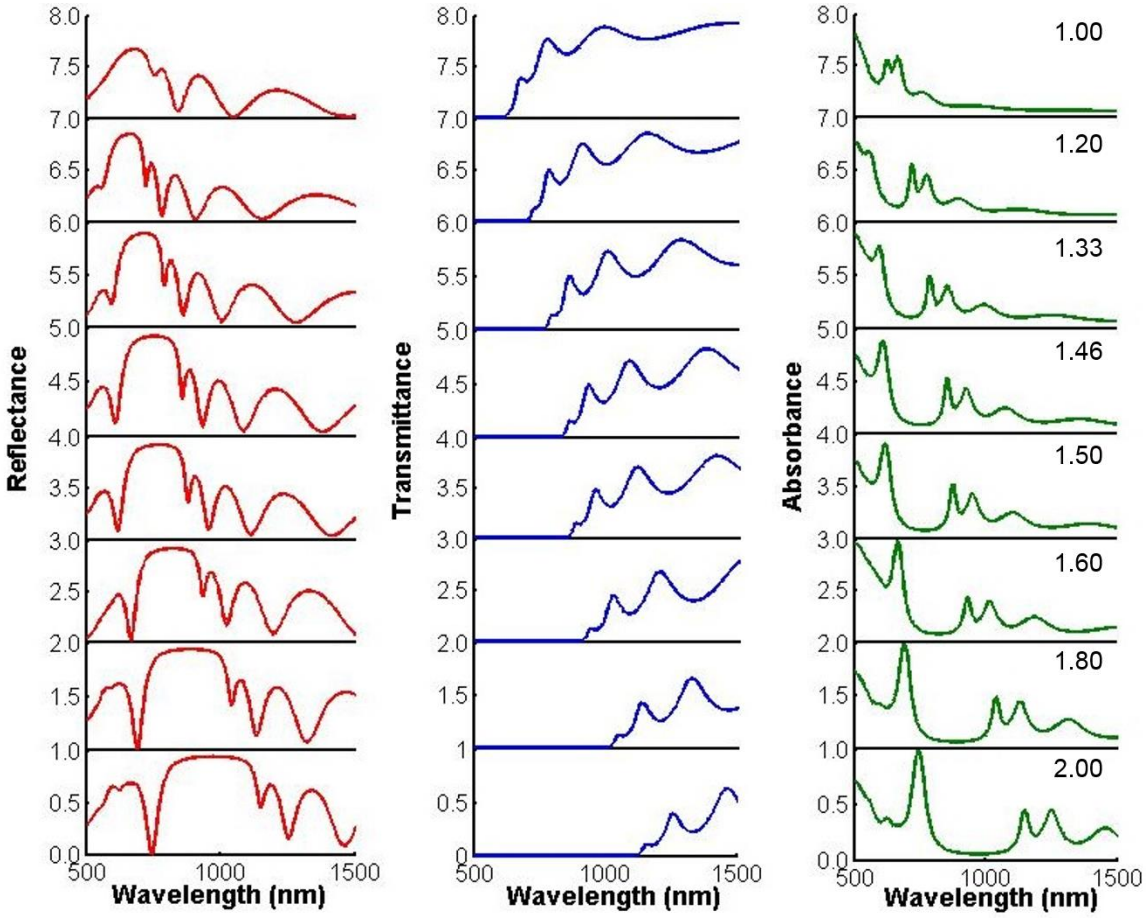

Fig. S48. Reflectance (left), transmittance (middle) and absorbance (right) spectra of superlattice with different dielectric media. The superlattice parameters are fixed, namely nanocubes with 88 nm edge length and 5 nm rounding, 134 nm lattice constant and 7 layers are used. The refractive index of the dielectric medium is shown on the top-right corner of the absorbance spectra.

15. References

1. Johnson PB,Christy RW (1972) Optical constants of the noble metals. *Phys Rev B* 6(12):4370-4379.
2. Shiles E, Sasaki T, Inokuti M, Smith DY (1980) Self-consistency and sum-rule tests in the Kramers-Kronig analysis of optical data: Applications to aluminum. *Phys Rev B* 22(4):1612-1628.
3. Hagemann HJ, Gudat W, Kunz C (1975) Optical constants from the far infrared to the x-ray region: Mg, Al, Cu, Ag, Au, Bi, C, and Al_2O_3. *J Opt Soc Am* 65(6):742-744.
4. Park DJ, *et al.* (2015) Plasmonic photonic crystals realized through DNA-programmable assembly. *Proc Natl Acad Sci USA* 112(4):977-981.
5. O'Brien MN, Jones MR, Brown KA, Mirkin CA (2014) Universal noble metal nanoparticle seeds realized through iterative reductive growth and xxidative dissolution reactions. *J Am Chem Soc* 136(21):7603-7606.
6. Jones MR, *et al.* (2010) DNA-nanoparticle superlattices formed from anisotropic building blocks. *Nat Mater* 9(11):913-917.
7. O'Brien MN, Lin HX, Girard M, de la Cruz MO, Mirkin CA (2016) Programming Colloidal Crystal Habit with Anisotropic Nanoparticle Building Blocks and DNA Bonds. *J Am Chem Soc* 138(44):14562-14565.
8. Senesi AJ, *et al.* (2014) Oligonucleotide flexibility dictates crystal quality in DNA-programmable nanoparticle superlattices. *Adv Mater* 26(42):7235-7240.
9. Macfarlane RJ, *et al.* (2011) Nanoparticle superlattice engineering with DNA. *Science* 334(6053):204-208.
10. Hurst SJ, Lytton-Jean AKR, Mirkin CA (2006) Maximizing DNA loading on a range of gold nanoparticle sizes. *Anal Chem* 78(24):8313-8318.
11. Auyeung E, *et al.* (2014) DNA-mediated nanoparticle crystallization into Wulff polyhedra. *Nature* 505(7481):73-77.
12. Auyeung E, Macfarlane RJ, Choi CHJ, Cutler JI, Mirkin CA (2012) Transitioning DNA-engineered nanoparticle superlattices from solution to the solid state. *Adv Mater* 24(38):5181-5186.
13. Butté R, *et al.* (2007) Current status of AlInN layers lattice-matched to GaN for photonics and electronics. *J Phys D* 40(20):6328.
14. Fowles GR (1975) *Introduction to Modern Optics* (Holt, Rinehart and Winston, New York) Second Ed.
15. Osting B (2012) Bragg structure and the first spectral gap. *Appl Math Lett* 25(11):1926-1930.
16. Jang SJ, Song YM, Yeo CI, Park CY, Lee YT (2011) Highly tolerant a-Si distributed Bragg reflector fabricated by oblique angle deposition. *Opt Mater Express* 1(3):451-457.
17. MRS BulletinArmstrong E,O'Dwyer C (2015) Artificial opal photonic crystals and inverse opal structures - fundamentals and applications from optics to energy storage. *J Mater Chem C* 3(24):6109-6143.
18. Waterhouse GIN,Waterland MR (2007) Opal and inverse opal photonic crystals: fabrication and characterization. *Polyhedron* 26(2):356-368.

19. Smith DR, Vier DC, Koschny T, Soukoulis CM (2005) Electromagnetic parameter retrieval from inhomogeneous metamaterials. *Phys Rev E* 71(3):036617.
20. Ho KM, Chan CT, Soukoulis CM (1990) Existence of a photonic gap in periodic dielectric structures. *Phys Rev Lett* 65(25):3152-3155.